Hindawi
Advances in Materials Science and Engineering
Volume 2022, Article ID 6160841, 25 pages
https://doi.org/10.1155/2022/6160841

Research Article

Flexural Behavior of Insulated Concrete Sandwich Panels using FRP-Jacketed Steel-Composite Connectors

Yi Wang,[1] **Jun Wang**,[1] **Donghui Zhao**,[2] **Gangarao Hota**,[3] **Ruifeng Liang**,[3] **and David Hui**[4]

[1]*College of Civil Engineering, Nanjing Tech University, Nanjing 211816, China*
[2]*The Fourth Construction Engineering Company Ltd. of China Construction Second Engineering, Tianjin 300457, China*
[3]*Department of Civil and Environmental Engineering, West Virginia University, Morgantown, WV 26506, USA*
[4]*Department of Mechanical Engineering, University of New Orleans, New Orleans, LA 70148, USA*

Correspondence should be addressed to Jun Wang; wangjun3312@njtech.edu.cn

Received 13 July 2022; Revised 9 October 2022; Accepted 11 October 2022; Published 2 November 2022

Academic Editor: Qi Cao

This study presented the experimental and theoretical results of insulated concrete Sandwich panels with innovative dumbbell-shaped steel fiber-reinforced polymer (FRP) composite bar (SFCB) connectors under flexural load. The influences of FRP thickness and raised thickness of dumbbell ends of connectors, axial compression ratio, the content of vitrified microspheres in the wythes, and loading direction were discussed. The increase in thickness of a glass FRP (GFRP) jacket on the hybrid bar from 2 to 3 mm led to increased initial cracking load, ultimate load, and flexural stiffness of the Sandwich panels by 75, 49, and 16%, respectively. The increase in the thickness of dumbbell ends from 4 to 6 mm led to increased initial cracking load, ultimate load, and flexural stiffness of the Sandwich panels of 18, 46, and 9%, respectively. The incorporation of vitrified microspheres in concrete wythes resulted in a significant increase in the load-carrying capacity of Sandwich panels but decreased ductility. Increased axial compression ratio from 0/1 to 0.2/1 contributed in improving the crack resistance and ultimate loads of Sandwich panels. Further increase of the axial compression ratio to 0.4/1 led to crushing failure of concrete wythe ends. Specimens under negative loads had higher ultimate loads than the counterparts under positive loads. Three-dimensional finite-element (FE) models were developed to simulate Sandwich panel flexural behavior and numerical results compared with the test data. Then, the verified FE model was used to analyze the influence of the arrangement of dumbbell-shaped SFCB connectors. Increased connector spacing from 550 to 650 mm was found to have an insignificant influence on load-deflection responses. Moreover, analytical solutions for deflection of Sandwich panels under combined axial-flexural load were obtained, in which the effect of slipping between the facade and structural wythes and shear deflection were considered. The predicted deflection at the ultimate load agreed well with the test results. This study provided a theoretical basis and design reference for FRP-jacketed steel-composite connectors in applications of Sandwich wall panels with large insulation layer thickness.

1. Introduction

Precast concrete sandwich panels with an insulation layer are increasingly used as exterior walls in buildings because of their energy conservation, convenient installation, and excellent thermal efficiencies [1]. A typical precast concrete wall-panel system consists of two reinforced concrete wythes, core insulation, and connectors penetrating through the insulation [2]. Precast concrete wall panels can be classified as fully composite, noncomposite, or partially composite. Practically all precast concrete panels in use are partially composite with stiffness depending on the configuration of the shear connectors [3]. To ensure sufficient composite action to meet design requirements of strength and stiffness, connectors between wythes should provide adequate shear transfer ability [4]. Steel shear connectors have been widely employed to hold the wythes and foam core together. However, huge heat losses are noted in sandwich wall panels with steel connectors, due to the thermal bridging effect caused by the steel [5, 6].

Nonmetallic connectors, such as fiber-reinforced polymer (FRP) connectors and plastic connectors, have been developed as alternatives to steel connectors. FRP not only has high tensile strength, low thermal conductivity but also has low elastic modulus and poor ductility. Combining the advantages of FRP and steel, hybrid FRP/steel connectors are expected to have high elastic modulus and shear strength, good ductility, and be cost-effective. In this study, an innovative dumbbell-shaped steel-FRP composite connector was developed and the flexural behavior of sandwich panels with these novel connectors was investigated to understand composite action and failure mechanisms. The effects of the configuration of connectors, axial compression ratio, loading direction, and content of vitrified microspheres in the wythes were considered. The resulting sandwich panels with these novel connectors were expected to be lightweight, have high composite action, and be energy-efficient for potential applications in prefabricated buildings in cold regions. The process is shown in the graphical abstract.

Researchers have investigated the design and properties of various shapes of FRP connectors. For example, Woltman et al. [7] have investigated three different kinds of connectors produced from glass FRP (GFRP) bars, in comparison with steel and polymer connectors. The shear strengths of these GFRP connectors (48–112 MPa) have been reported to be much higher than those of specialized polymer connectors (22–39 MPa), but lower than those of steel connectors (297–365 MPa). Chen et al. [8] compared the flexural behavior of concrete sandwich panels with different types of FRP plate connectors, in which the continuous and segmental connectors perform much better than discrete connectors. Tomlinson et al. [9] compared the behavior of basalt FRP (BFRP) and steel connectors under push-through loads. Their results showed the BFRP and steel connectors had similar tensile strength for diameters of 6 mm, while the compressive strength of steel connectors was double than that of BFRP connectors. Lameiras et al. [10] investigated the influence of different laminates and the number and geometry of holes of perforated GFRP plate connectors and found that the ultimate pull-out load capacities of connections with 3 holes (hole diameter and spacing at 30 and 45 mm, respectively) increased 49% compared with connections without holes. Choi et al. [11] investigated the inplane shear behavior of concrete sandwich panels with grid-type GFRP composites. Their results showed reductions in panel stiffness with increases in grid spacing of extruded polystyrene (XPS) insulation. Although sandwich wall panels with FRP grids or continuous connectors usually have a higher degree of composite action than wall panels with separate FRP connectors. A separate FRP connector has a relatively small cross section and can be simply designed and commercially constructed [12]. Therefore, separate FRP connectors have been recently used extensively in sandwich insulation wall panels. Separate FRP connectors usually adopt groove or angled features and both ends of FRP connectors can be grooved to increase friction between the connectors and concrete wythes [13]. This anchorage effect relies on construction quality [14], connectors arranged at an angle can better utilize the axial stiffness of the materials [9], and the insertion angle and diameter of FRP connectors have significant effects on the ultimate capacity and stiffness of sandwich wall panels. FRP plate and FRP tube connectors can use anchorage rebars passed through perforated plates and tubes to improve anchorage effects [12, 15]. Although using FRP connectors is beneficial for thermal insulation purposes, the low elastic modulus and shear strength as well as the brittle failure type hinder the widespread application of FRP connectors.

Hybrid FRP/steel connectors combine the advantages of the two materials. Wu et al. [16] have developed a novel hybrid steel-FRP composite bar (SFCB) which consists of a steel core and FRP jacket. SFCBs exhibit bilinear tensile stress-strain curves before fracture and have stable post-yield stiffness after yielding [16]. Cleary et al. [17] incorporated FRR plates into steel connections to correct thermal bridging issues. Dong et al. [18] investigated bond durability between SFCBs and sea sand concrete in an ocean environment. Their test results indicated that chloride ions in sea sand improved SFCB bonding within the test duration (90 d) and the degree of corrosion in continuous immersion is greater than that in a wet-dry cycling environment. Seo et al. [19] compared the tensile properties of glass-type SFCBs with different steel cores, including a steel rod, a bunch of steel wires, or steel rebar in the core. SFCBs with a steel wire core exhibit the highest tensile strength than other composite bars. Zhi and Guo [20] stated that a reasonable design of *W*-shaped SFCB connectors could provide high composite action for Sandwich panels and enhance panel ductility due to steel cores in the connectors. Zhou et al. [21] examined SFCB durability by *X*-ray microcomputed tomography and found actual corrosion rates of carbon-type and glass-type SFCBs were less than 10 and 1% of the corrosion rate when compared with an ordinary steel bar, respectively. Yang et al. [22] reported the flexural behavior of concrete beams reinforced by SFCBs, in which SFCB-reinforced concrete beams display completely different failure modes compared with RC beams, depending on the reinforcement ratio and steel/FRP ratio [22]. Concrete beams reinforced with steel-BFRP composite bars exhibit better ductility and smaller crack widths compared with the beams reinforced with steel-GFRP composite bars [23]. Previous studies have indicated that SFCBs can be produced industrially and cost-effectively [24]. SFCB connectors possess superior performance in terms of stiffness and load-carrying capacity [25]. However, because FRP adhesion to concrete is not as high as that of steel, some form of mechanical anchorage should be provided for SFCB connectors [26].

The objective of this study was to develop an innovative dumbbell-shaped SFCB connector and study its effects on the flexural behavior of insulated concrete sandwich panels. FRP thickness, raised thickness of dumbbell ends of connectors, axial compression ratio, and content of vitrified microspheres in the wythes were varied to investigate the structural behavior of these sandwich panels. The incorporation of a certain content of vitrified microspheres in concrete as lightweight aggregates was aimed to reduce the overall panel weight. Furthermore, when these sandwich panels are applied as external wall panels of high-rise

buildings, they should have sufficient resistance against frontal wind pressure (positive pressure) and backwind suction (negative pressure). Thus, the flexural behavior of these panels under positive and negative loads was investigated. Then, finite-element (FE) models were constructed and the numerical results compared with the experimental data were gathered here. The verified FE model was finally used to investigate the influence of shear connector arrangement. In addition, an analytical model was developed and presented to predict the deflection of these panels under combined axial-flexural loads.

2. Experimental Program

2.1. Details of Proposed Connectors. Connectors were designed based on hybrid GFRP-steel bars and fabricated by pultrusion. Crescent-rib steel rebar with an 8 mm diameter was used as the core material for the connectors. The manufacturing process of the hybrid GFRP-steel bars has been previously described [16]. A 25 mm length at the top and bottom of the hybrid FRP-steel bars was wrapped with six or nine layers of GFRP to prevent slippage between the concrete wythe and shear connector. All shear connectors were of the same 250 mm length. The differences between the shear connectors were the thickness of GFRP and the raised thickness of the dumbbell ends. The thickness of GFRP jackets of hybrid bars varied from 2 to 3 mm and the raised thickness of dumbbell ends varied also from 4 to 6 mm.

2.2. Material Properties. E-glass rovings and vinyl ester resin were used to produce hybrid GFRP-steel bars. Moreover, the dumbbell ends were composed of E-glass woven fabric with vinyl ester resin. The volume ratio of the glass fiber was 65%. The mechanical properties of glass fiber obtained from the manufacturer were tensile strength 750 MPa, compression strength 725 MPa, and Young's modulus 45 GPa. Vinyl ester resin had physical performance indices of tensile strength 55 MPa, fracture elongation 2%, and flexural strength 105 MPa. The tensile strength and Young's modulus of GFRP obtained from the manufacturer were 360 MPa and 25 GPa, respectively. HRB335 steel bars, with a yield strength of 335 MPa and Young's Modulus of 200 MPa, were used in the production of hybrid GFRP-steel bars.

The tensile and shear properties of the hybrid GFRP-steel bars were measured in accordance with GB/T 228.1-2010 [27] and JG/T 406-2013 [28]. The pull-out strength of the dumbbell-shaped SFCB connector to concrete was measured in accordance with GB/T 50081-2019 [29]. The measured properties of shear connectors are given in Table 1.

Graphite polystyrene (GPS) foam was used as insulation, which could be effective against moderate fire exposure because of its low thermal conductivity and class B fire resistance (flame spread rating between 26 and 75). The properties of GPS foam provided by the manufacturer were density 23.5 kg/m^3, compressive strength 117 KPa, and thermal conductivity coefficient 0.034 W/(m·K).

Vitrified microspheres are a type of inorganic insulation material with vitrified irregular closed surfaces and porous microstructures, obtained from glass lava ore by vitrification. Their particle size is in the range of 0.5–1.5 mm and their bulk density is 300 kg/m^3. The incorporation of vitrified microspheres in concrete contributed to decreasing concrete density and thermal conductivity of concrete [30]. However, excessive vitrified microspheres might lead to decreased concrete compressive strength and elasticity modulus. Previous research by Zhao et al. [31] indicated microcracks that occur around microspheres once the mass ratio increases to 2.8%. Therefore, the mass ratios of vitrified microspheres to concrete mixture mass were chosen here as 0, 0.6, and 1.2% (corresponding volume fractions were 0, 10, and 20%, respectively). For concrete with certain microsphere content, five 150 mm cubes were cast and cured under conditions similar to those of the related Sandwich panels. The compressive properties of the concrete are shown in Table 2.

Wire mesh with a diameter of 8 mm was used for flexural reinforcement of the concrete wythe. The yield strength and elastic modulus of the steel wire mesh were 400 MPa and 210 GPa, respectively.

2.3. Test Specimens. Nine specimens were prepared to study the flexural responses of Sandwich panels with dumbbell-shaped SFCB connectors. The fabrication procedure of Sandwich panel specimens is shown in Figure 1. Two layers of steel wire mesh in the structural wythe were first installed. Then, the shear connectors were bound to the steel mesh at the design positions. After casting the concrete in the structural wythe, the insulation foam was installed, in which the shear connectors penetrated the foam. After that, the steel wire mesh in the facade wythe was installed, followed by casting the concrete in the façade wythe. The Sandwich panel specimens and molds were covered with plastic film to prevent moisture loss and then cured at room temperature for 24 h. After removal from their molds, the specimens were cured in a standard curing room at $20 \pm 2^{\circ}$C at a relative humidity (RH) of 95% for 28 d.

The proposed wall was a 2800×1000 mm Sandwich panel system with a total thickness of 310 mm. All specimens consisted of a 120-mm-thick structural wythe, a 60-mm-thick facade wythe, and a 130-mm layer of GPS foam insulation between the two wythes. This thickness of insulation was aimed to achieve the desired thermal efficiency in cold regions of China (heat transfer coefficient of external wall ≤ 0.35 W/(m^2·K)). The facade and structural wythes were reinforced with one and two layers of 8 mm-diameter steel welded wire mesh (bar spacing of 250 mm in longitudinal direction and 150 mm in transverse direction), respectively. The spacing of shear connectors was 600 mm in longitudinal and transverse directions. The shear connectors of the control specimen had 2-mm-thickness of GFRP on the hybrid bars and 4 mm raised thickness of dumbbell ends. The reference specimen was forced to yield a positive moment. The arrangements of the steel reinforcements and connectors are shown in Figure 2.

Table 1: Mechanical properties of the shear connectors.

Properties	Connector 1	Connector 2	Connector 3
Tensile strength (MPa)/δ (%)	492/4.8	521/3.8	492/6.8
Tensile modulus (GPa)/δ (%)	65/4.5	49/5.2	65/3.5
Shear strength (MPa)/δ (%)	337/2.5	302/2.4	337/2.5
Pull-out load capacity (kN)/δ (%)	23.8/2.5	22.4/4.9	26.5/3.0

Note. The thickness of FRP jacket and raised thickness of dumbbell ends of connector 1 are 2 mm and 4 mm, respectively, the thickness of FRP jacket and raised thickness of dumbbell ends of connector 2 are 3 mm and 4 mm, and the thickness of FRP jacket and raised thickness of dumbbell ends of connector 3 are 2 mm and 6 mm, respectively, and δ is coefficient of variation.

Table 2: Concrete compressive properties.

Properties	Concrete 1	Concrete 2	Concrete 3
Volume fractions of vitrified microspheres	0%	10%	20%
Density (kg/m^3)	2492	2424	2365
Compressive strength (MPa)/δ (%)	28.4/3.3	32.6/3.6	35.3/2.5
Compressive modulus (GPa)/δ (%)	29.0/4.5	33.0/5.2	34.5/4.7
Poisson's ratio	0.2	0.2	0.2

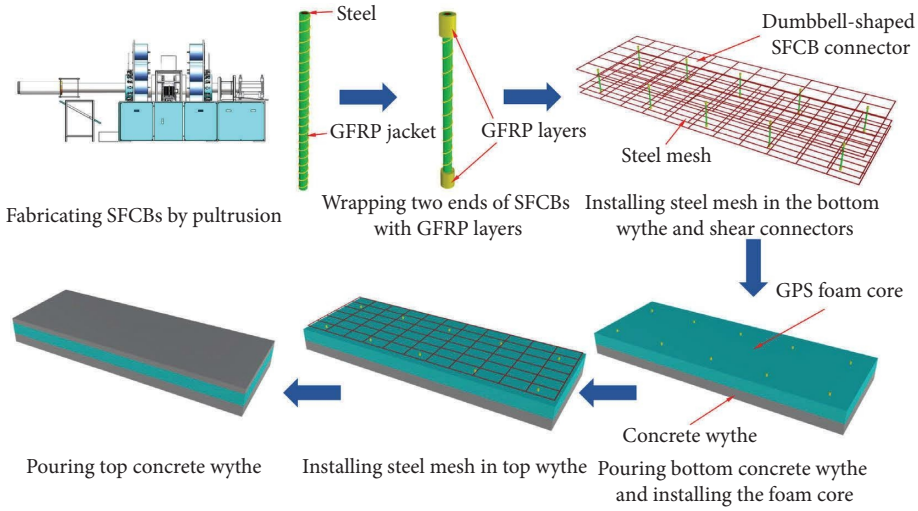

Figure 1: Fabrication procedure of insulated sandwich panels using dumbbell-shaped SFCB connectors.

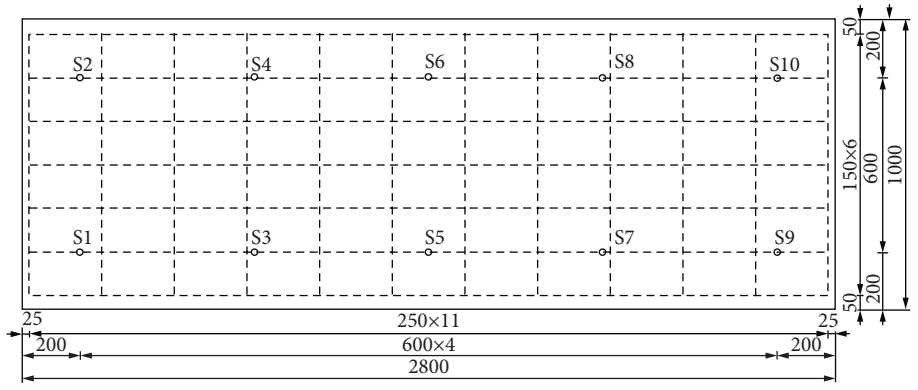

(a)

Figure 2: Continued.

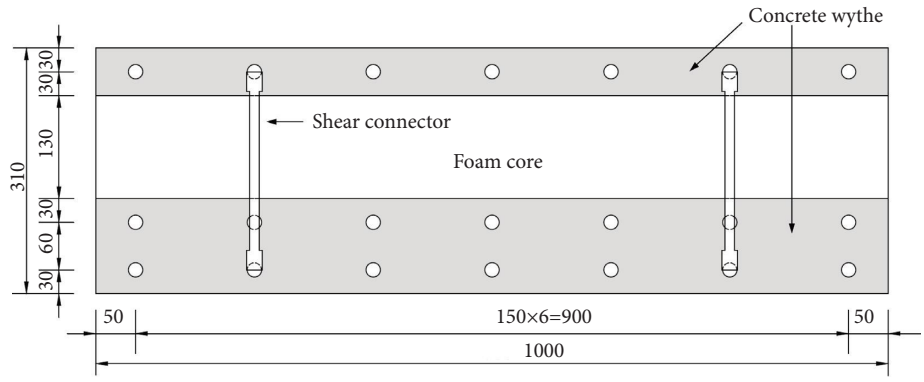

(b)

(c)

Figure 2: The arrangement of the steel reinforcements and connectors (units: mm). (a) Top view of the sandwich panel. (b) Cross section of the sandwich panel. (c) Dumbbell-shaped SFCB connectors.

The details of the test specimens are provided in Table 3. A list of the main parameters investigated are as follows: (1) GFRP thickness on the hybrid bars varied from 2 to 3 mm and raised thickness of the dumbbell from 4 mm to 6 mm. (2) Vitrified microsphere volume fractions of concrete wythes varied between 0, 10, and 20%. (3) Axial loading was applied on two specimens under combinations of flexural and axial loads, with the axial compression ratio varying between 0/1, 0.2/1, and 0.4/1. The axial compression ratio is $n = C_0/(f_c A_c + f_{ya} A_a)$, with C_0 the applied axial compression force of Sandwich panels, f_c the prismatic compressive strength of concrete, with $f_c = 0.76\, f_{cu}$, f_{cu} the cubic compressive strength of concrete, A_c the gross cross-sectional area of concrete wythes, f_{ya} the yield strength of steel reinforcements, and A_a the cross-sectional area of steel reinforcements in the longitudinal direction in the facade and structural wythes. (4) The loading direction of 7 specimens was loaded out of the plane on the facade wythe to simulate external wind pressure and two specimens were loaded out of the plane on the structural wythe to simulate suction pressure (Figure 3).

2.4. Experimental Set-Up. Specimens were tested under a four-point bending condition with load acting at one-third intervals of the span. The experimental set-up consisted of a 200 kN load cell, which transferred the load to two load heads using a rigid steel spreading beam. The clear span was kept at 2600 mm for each Sandwich wall panel. Linear variable displacement transducers (LVDTs) were used to monitor the deflections at the supports and bottom deflection at the midspan. The test set-up of four points simply supported Sandwich panels (Figure 4). The stress state of the midspan cross section was monitored by strain gauges A1 to A5, which were bonded to the steel wires in the facade wythe, and strain gauges B1 to B5 and C1 to C5 were bonded to the steel wires in the structural wythe, with gauge 10 mm in length (Figure 5). A load interval within one-fifteenth of the estimated failure load capacity was taken and maintained while testing for 10 min until the gauge readings became stable. Tests were stopped till the panels were fractured.

3. Test Results and Discussion

3.1. General Behavior and Failure Mode. Typical failure modes are shown in Figure 6. The reference specimen G24-I exhibited liner-elastic behavior in the early stage and, as the load increased up to ~35% of the ultimate load, vertical cracks occurred on the facade wythe near the loading point. Further increased load up to 90% of the ultimate load caused several vertical cracks at the structural wythe of the midspan. The facade wythe completely bonded with the foam core during the test, while an end slip occurred between the

Table 3: Details of test specimens.

Specimen	Thickness of GFRP on hybrid bars (mm)	Raised thickness of dumbbell ends (mm)	Volume fraction of vitrified microspheres (%)	Axial compression ratio	Loading direction
G24-I	2	4	0	0	Positive
G24-II	2	4	0	0	Negative
G24S10-I	2	4	10	0	Positive
G24S20-I	2	4	20	0	Positive
G24A0.2-I	2	4	0	0.2	Positive
G24A0.4-I	2	4	0	0.4	Positive
G34-I	3	4	0	0	Positive
G26-I	2	6	0	0	Positive
G26-II	2	6	0	0	Negative

Note. In the first column, the first letter *G* means GFRP-steel hybrid connectors are used in Sandwich panels, the first and second numbers mean the thickness of GFRP on hybrid bars and raised thickness of dumbbell ends, the second letter *S* and *A* mean vitrified microspheres are added in concrete and axial compression load is applied on the panels, respectively, the numbers 10 and 20 after the letter *S* mean the volume fractions of vitrified microspheres are 10% and 20%, respectively, the number 0.2 and 0.4 after the letter *A* mean the axial compression ratios of the panels, respectively, and the last number I and II mean the load results in positive and negative moments in the panels, respectively.

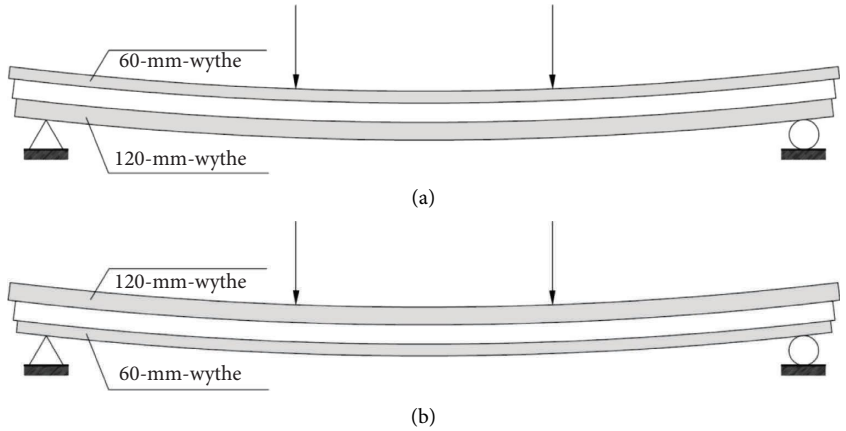

Figure 3: Diagram of deformed sandwich panels under (a) positive loads and (b) negative loads.

Figure 4: Test set-up. (a) Four-point flexural test and (b) axial loading device.

structural wythe and foam core. The inclined shear cracks in the foam propagated to the facade wythe and the specimen deflection increased rapidly without increased load. This specimen finally failed with penetrating cracks on the bottom of the structural wythe of the midspan. The thickness of GFRP on the hybrid bars, raised thickness of the dumbbell, and the content of vitrified microspheres had insignificant influences on the failure modes of the tested Sandwich panels. Meanwhile, the flexural cracks on the facade wythe near the loading point developed more slowly for Sandwich panel specimens with thicker GFRP on the hybrid bars and higher content of vitrified microspheres.

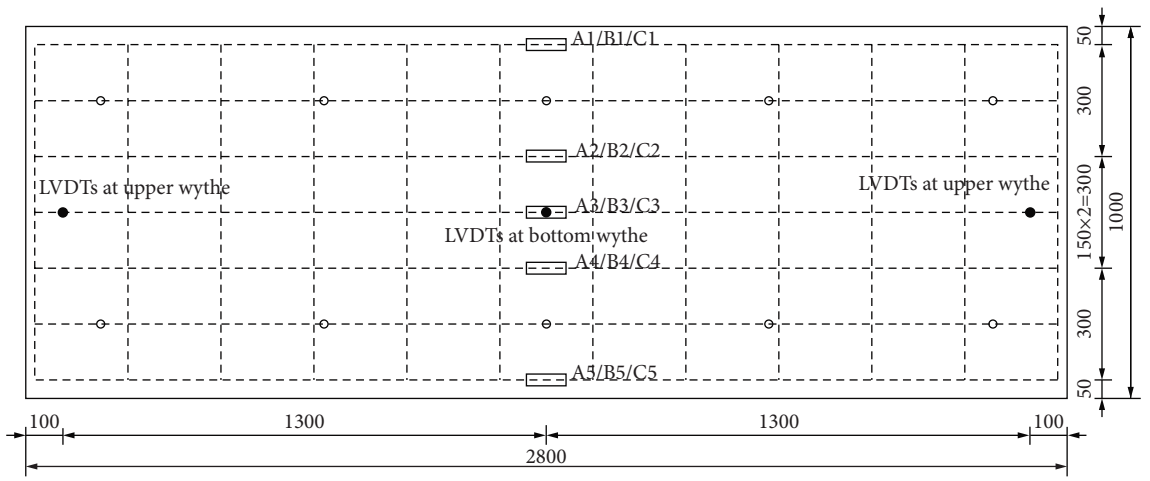

Figure 5: Strain gauge arrangement on the steel reinforcements and LVDT arrangement on the wythes (units: mm).

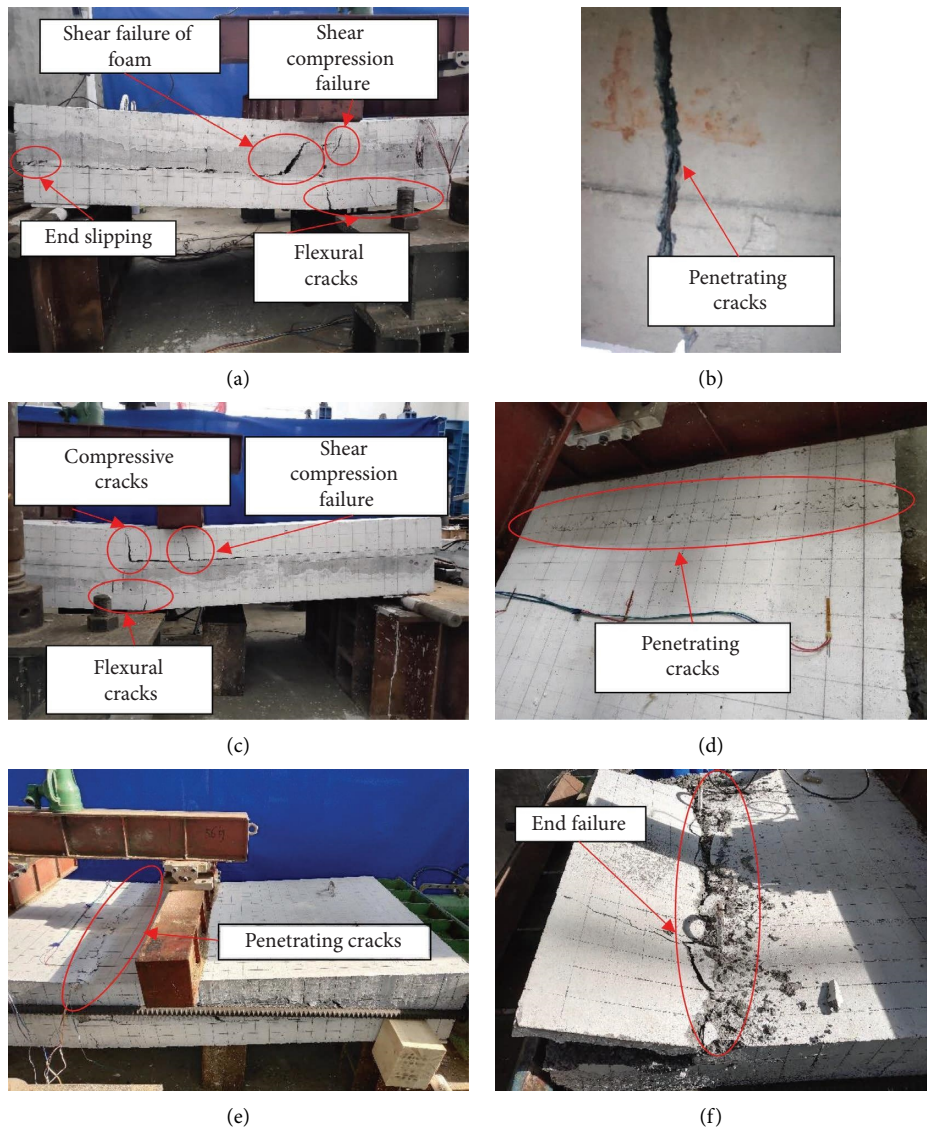

Figure 6: Failure modes of tested Sandwich wall panels. (a) Side view of specimen G24-I, (b) back of bottom wythe of specimen G24-I, (c) side view of specimen G24-II, and (d) vertical view of top wythe of specimen G24-I, (e) specimen G24A0.2-I, and (f) specimen G24A0.4-I.

The specimens under the combined effects of axial and flexural loads and the specimen under negative loads exhibited different failures with specimen G24-I. The axial compressive load contributed to the delay in the onset of concrete cracks. The tensile crack occurred on the structural wythe of the specimen with an axial compression ratio of 0.2/1 while the vertical load increased up to ~80% of the ultimate load. This was followed by cracks occurring on the facade wythe of the specimen and then failure by penetrating cracks on the face of the façade wythe of the midspan. For specimens with an axial compression ratio increased to 0.4/1façadefacade wythe peeled from the foam core and, then the end of the facade wythe was suddenly crushed. The cracking load of the specimens subjected to negative loads was ~60% of the ultimate loads and their failure modes were similar to those of specimens with an axial compression ratio of 0.2/1.

3.2. Load-Deflection Responses. The load-deflection curves for the test specimens at midspan showed that all specimens had high initial stiffness followed by cracking and gradually reduced stiffness before the ultimate load and onset of failure (Figure 7). These Sandwich panels exhibited considerable ductility evidenced by a large amount of midspan deflection.

The increase in thickness of the GFRP jacket on hybrid bars from 2 to 3 mm (G24-I and G34-I) led to increased initial cracking load, ultimate load, and flexural stiffness (slope of the load-deflection curve in the linear-elastic phase) of the Sandwich panels by 75, 49, and 16%, respectively. Compared with specimen G24-I, the absorbed energy of G34-I increased by 22%, while the ductilities of these two specimens were almost identical. Herein, the absorbed energy was calculated from the area under the load-deflection curve before a sudden drop in the load. The ductility factor was defined as the maximum deflection divided by the corresponding deflection when yielding occurred [32]. Increasing the thickness of the GFRP jacket was found to increase load-carrying capacity and flexural stiffness, as well as energy absorption because of thicker fiber layers resulting in extra confinement to steel bars.

The increased raised thickness of dumbbell ends from 4 to 6 mm (G24-I and G26-I) led to increased initial cracking load, ultimate load, and flexural stiffness of the Sandwich panels of 18, 46, and 9%, respectively. Compared with specimen G24-I, the absorbed energy increased by 26% and ductility decreased by 14% for G26-I. Increasing the raised thickness of dumbbell ends contributed to improved integration performance of these panels.

The increased volume fraction of vitrified microspheres, from 0 to 10 and 20%, led to an increased initial cracking load of the panels by 49 and 72%, respectively, and an increase in ultimate load by 33 and 45%, increased flexural stiffness by 25 and 50% and increased absorbed energy by 37 and 57%, respectively. However, the incorporation of vitrified microspheres in concrete wythes led to decreased ductility, which might have been attributable to the brittle nature of these microspheres.

An increase in axial compression ratio from 0/1 to 0.2/1 led to increased initial cracking load, ultimate load, and absorbed energy of the Sandwich panels, by 205, 142, and 157%, respectively. Compressive loads contributed to decreased tensile stress in the bottom wythes, thus improving specimen crack resistance and load-carrying capacity. Before crack initiation in the concrete, axial compressive loads had no influence on specimen flexural stiffness. A clear decrease in ductility was observed in specimens under combined axial-flexural loading. After reaching the ultimate load, a load of specimens under combined axial-flexural loading decreased continuously. Consequently, the ratio of the ultimate deflection to yield deflection decreased and thus ductility decreased.

The observed effects of loading direction on mechanical properties of the Sandwich panel specimens (G24-I vs. G24-II, and G26-I vs. G26-II) showed that specimens under negative loads had higher initial cracking load than specimens under positive loads. This was because the distance from the neutral axis to the bottom of panel specimens under negative loads was larger than that of specimens under positive loads, leading to lower tensile stress in the former. Consequently, the flexural capacity of specimens under negative loads was higher than that of specimens under positive loads, and the yield deflection of the former was higher than that of the latter. Therefore, the ductility of specimens under negative loads was lower than that of specimens under positive loads. Specimen flexural stiffnesses in the elastic phase were independent of the loading direction. The absorbed energy of specimen G24-II was higher than that of G24-I, while the absorbed energy of G26-II was higher than that of G26-I. The loading direction had an insignificant effect on the ultimate load of specimens with a 6 mm raised thickness of dumbbell ends, while the maximum deflection in G26-II was smaller than that of G26-I, resulting in lower absorbed energy in G26-II.

Both the increased thickness of FRP jackets and the thickness of dumbbell ends contributed to increasing the decrease in the slip between the two wythes, while increased vitrified microsphere content led to a slight increase in the slip between the two wythes. No slip occurred in specimens under combined axial-flexural loading. The test results are summarized in Table 4.

3.3. Load-Strain Responses. The progressive development of longitudinal strains of reinforcements at the midspan of typical specimens was examined. The two layers of reinforcements in tension in the bottom wythe were consistently found to yield in specimens under positive loads, while the compressive strain of reinforcements in the upper wythe was small until specimen failure (Figures 8(a) and 8(b)). At the same loading level, the strain of the outermost reinforcements in tension was higher than that of the innermost reinforcements. For specimens under negative loads, reinforcements in tension yielded, while strains in the two layers of reinforcement in compression were small under fairly high loading levels (Figure 8(c)).

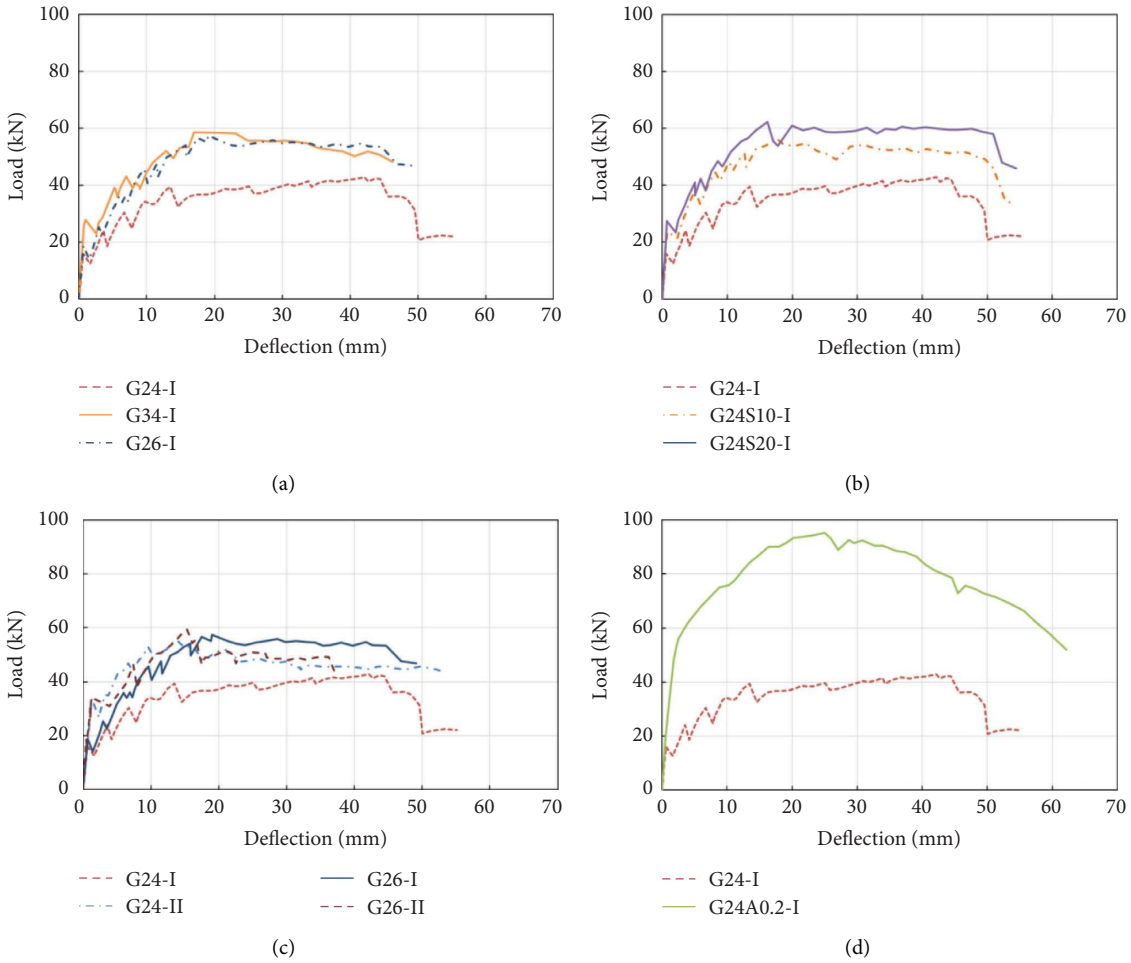

Figure 7: Load-deflection curves. (a) Specimens with different thicknesses of FRP jacket and dumbbell. (b) Specimens with different contents of vitrified microspheres. (c) Specimens under different load directions. (d) Specimens with different axial compression ratios.

Table 4: Test results.

Specimen	Cracking load (kN)	Ultimate load (kN)	Stiffness (kN/mm)	Deflection at the ultimate load (mm)	Slip at the ultimate load (mm)	Ductility	Absorbed energy (J)
G24-I	15.87	39.44	25.06	13.47	11	26.62	1876.62
G24-II	33.76	55.41	25.71	13.88	20	22.24	2430.66
G24S10-I	23.68	56.66	31.27	17.41	13	21.84	2567.05
G24S20-I	27.35	62.19	37.61	16.22	15	24.82	2942.33
G24A0.2-I	48.40	95.25	26.44	25.00	0	13.23	4826.09
G34-I	27.82	58.59	29.09	16.98	2	26.00	2285.06
G26-I	18.75	57.45	27.35	19.05	5	30.38	2364.81
G26-II	34.18	59.31	27.94	15.33	10	25.70	1724.37

3.4. Estimation of Degree of Composite Action. The degree of composite action for Sandwich wall panel specimens can be estimated in terms of the initial stiffness and ultimate strength [33], expressed as

$$\kappa_1 = \frac{I_{\exp} - I_{nc}}{I_c - I_{nc}} \times 100. \quad (1)$$

and

$$\kappa_2 = \frac{P_{\exp} - P_{nc}}{P_c - P_{nc}} \times 100, \quad (2)$$

where, $I_{\exp}$, I_c, and I_{nc} are the experimentally-determined moment of inertia, theoretical moments of inertia for uncracked full and noncomposite action, respectively, and $P_{\exp}$, P_c, and P_{nc} are the experimental ultimate load, theoretical ultimate loads for full, and noncomposite action, respectively.

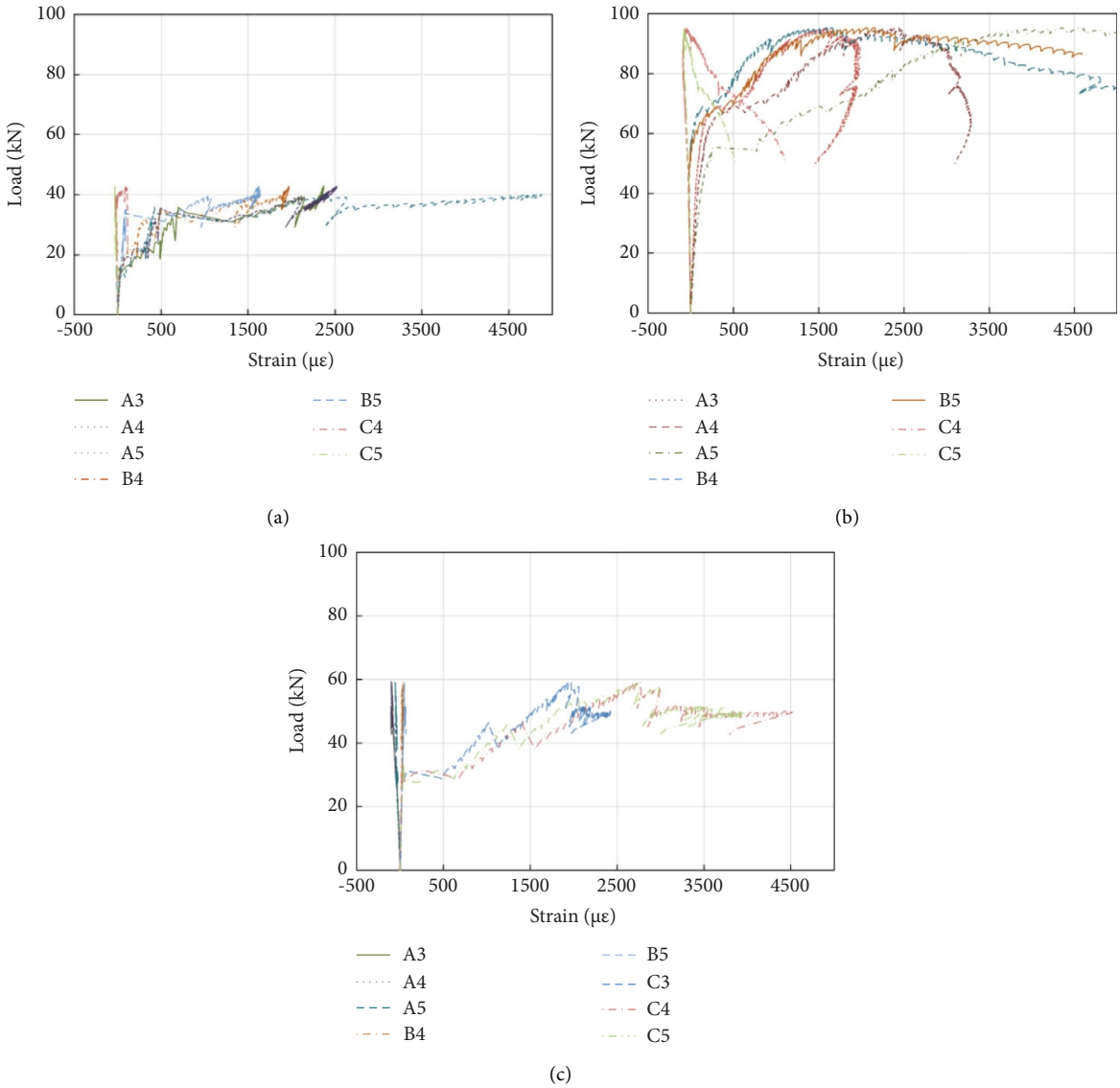

Figure 8: Typical load-strain curves of longitudinal reinforcement at the mid-span. (a) Specimen G24-I, (b) specimen G24A0.2-I, and (c) specimen G26-II.

The estimated values of the degree of composite action in terms of initial stiffness of the Sandwich panels with separate hybrid connections were in the range of 19 to 42. These were similar to those values of Sandwich panels with continuous GFRP grid connectors in Reference [34] (Table 5). This indicated that the facade and structural wythes behaved in a partially composite manner. The values of the degree of composite action in terms of ultimate strength were higher than those of values in terms of initial stiffness. Thicker FRP jackets and dumbbell end of connectors, the increased contents of vitrified microspheres in concrete wythes, and applied axial compressive load led to higher degrees of composite action. Moreover, specimens under negative loading had a much higher degree of composite action in terms of ultimate strength than specimens under positive loading.

4. Finite Element Simulation

A three-dimensional (3D) FE model was developed using Abaqus/Explicit to simulate the flexural responses of test specimens. Then, the verified FE model was used to analyze the arrangement of dumbbell-shaped SFCB connectors.

4.1. Material Models. The damaged plasticity model was used for concrete and the compressive properties of concrete were obtained from coupon testing (Table 2). The tensile strength of the concrete was taken as 10% of the compressive strength. The compressive and tensile stress-stain curves for concrete based on experimental results were determined according to GB 50010-2010 [35], and plotted in Figures 9 and 10. The compressive damage factor (d_c), tensile damage

Table 5: Degree of composite action.

Specimen	Degree of composite action in terms of initial stiffness			Degree of composite action in terms of ultimate strength		
	Cracking load (kN)	Deflection at the cracking load (mm)	κ_1 (%)	Theoretical ultimate load for full composite (kN)	Theoretical ultimate load for noncomposite (kN)	κ_2 (%)
G24-I	15.87	0.63	19	79.87	21.67	31
G24-II	33.76	1.10	26	60.40	21.67	87
G24S10-I	23.68	0.64	28	80.18	22.06	60
G24S20-I	27.35	0.63	32	80.35	22.26	69
G24A0.2-I	48.4	1.23	35	161.36	26.91	51
G34-I	27.82	0.61	42	79.87	21.67	63
G26-I	18.75	0.58	28	79.87	21.67	61
G26-II	34.18	1.22	23	60.40	21.67	97

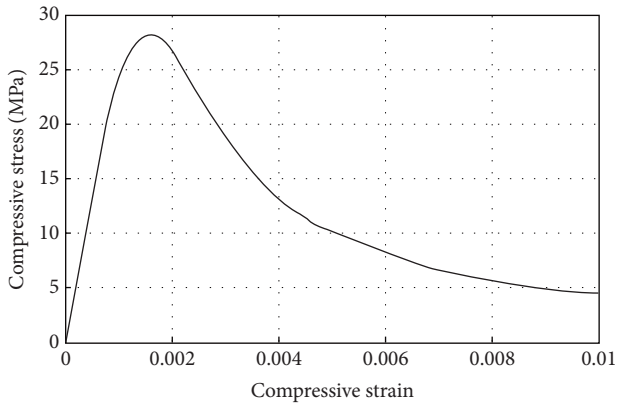

Figure 9: Compressive stress-strain curve of concrete.

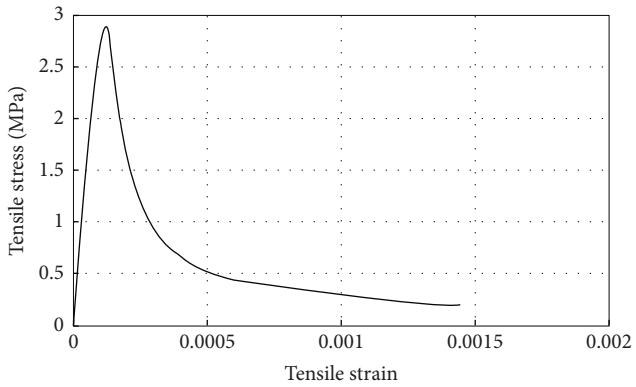

Figure 10: Tensile stress-strain curve of concrete.

factor (d_t), compressive inelastic strain (ε_c^{in}), and tensile cracking strain (ε_t^{ck}) were thus obtained according to [36] and incorporated in a damage plasticity model. Concrete mechanical parameters are listed in Table 6.

The steel reinforcement and steel core in shear connectors were assumed as elastic-plastic materials with a yield strength of 400 MPa and elastic modulus of 210 GPa. Linear elastic models were used for the insulation and GFRP on shear connectors and Hashin's criterion was applied to predict GFRP failure.

4.2. FE Model Construction. Eight-node reduced-integration continuum 3D solid elements (C3D8R) were used to model concrete panels, shear connectors, and insulation, and 3D 2-node first-order truss elements (T3D2) were used to model steel reinforcement. Based on the convergence study, the mesh sizes of the elements were 25 mm for the concrete panel, 13 mm for the connector, and 50 mm for the insulation and steel reinforcement. The mesh at the contact zone between shear connectors and concrete wythe and insulation was set to be finer to capture interactions between these elements (Figure 11).

The load was applied step by step using the full Newton method with NLGEOM in, which large-deflection effects were considered. The test specimens were simply supported and surface-to-surface contact elements were used to simulate the interface between concrete wythe and insulation. This type of contact considers slip and separation. Hence, slip/debonding was displayed if either occurred between the concrete wythe and insulation. Godrich et al. [37] stated that the friction coefficient within the range of 0–0.5 had an insignificant effect on the panel connection response. Jiang and Chorzepa [38] suggested that the friction coefficient for the contact surfaces of polymer composite and concrete can be taken as 0.22. Hence, the friction coefficient here was set as 0.22 for the contact surface of the wythe and insulation.

4.3. Comparison of Numerical and Experimental Results. The simulated failure modes and contours of stress, strain, and displacement of typical Sandwich panel specimens (i.e., G24-I and G24A0.2-I) are shown in Figures 12 and 13. For specimen G24-I, several tensile cracks occurred on the bottom wythe in the midspan, with a few cracks scattered at the loading point on the upper wythe and at supporting points on the bottom wythe. For G24A0.2-I, several tensile cracks occurred on the upper wythe due to the localized effect of the load applied at the midspan. The tension damage in the bottom wythe of G24A0.2-I was more serious than that of G24-I. The maximum Von Mises stress of the longitudinal rebars in the upper wythe and outermost longitudinal rebars in the bottom wythe was a little higher than the yield strength of rebar, indicating that these rebars

Table 6: Parameters of concrete mechanical behavior.

x_c	Compressive stress σ_c	Compressive inelastic strain ε_c^{in}	Compressive damage factor d_c	x_t	Tensile stress σ_t	Tensile cracking strain ε_t^{ck}	Tensile damage factor d_t
0.5	20.997244	0.000000	0.000000	0.6	2.052695	0.0000000	0.000000
0.8	27.292009	0.000339	0.142540	0.8	2.621428	0.0000056	0.029636
1	28.304000	0.000624	0.218975	1	2.888400	0.0000204	0.088956
1.5	23.391735	0.001593	0.420269	2	1.250389	0.0001969	0.576144
2	17.364417	0.002601	0.567430	3	0.752683	0.0003340	0.731492
3	10.561194	0.004435	0.724553	6	0.373373	0.0007071	0.866276
6	4.528640	0.009443	0.872459	10	0.241147	0.0011917	0.916756
9	2.841767	0.014302	0.917507	20	0.140553	0.0023952	0.955061
15	1.620705	0.023944	0.951744	40	0.084472	0.0047971	0.975365
20	1.192098	0.031959	0.964158				

Note. x_c is the ratio of the real compressive strain of concrete to the compressive strain of concrete corresponding to the compressive strength, and x_t is the real tensile strain of concrete to the tensile strain of concrete corresponding to the tensile strength.

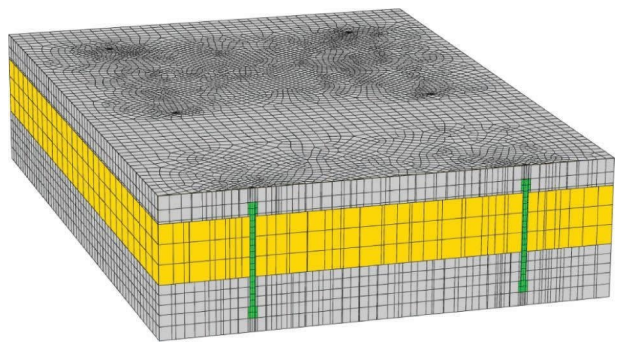

Figure 11: Finite element mesh.

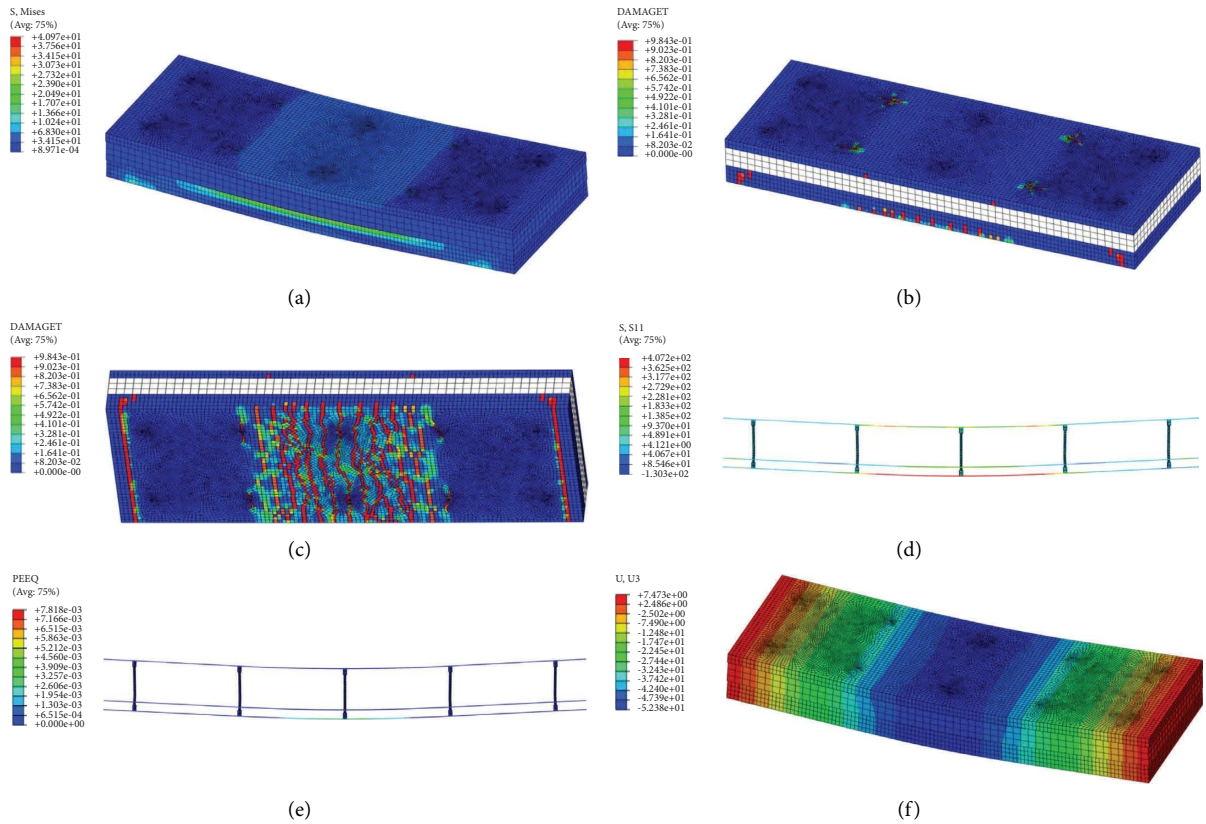

Figure 12: Simulated damage and contours of stress, strain, and displacement of G24-I at failure. (a) Stress contour of G24-I, (b) tension damage of G24-I, (c) tension damage on bottom wythe of G24-I, (d) stress contour of steel mesh of G24-I, (e) strain contour of steel mesh of G24-I, and (f) displacement contour of G24-I.

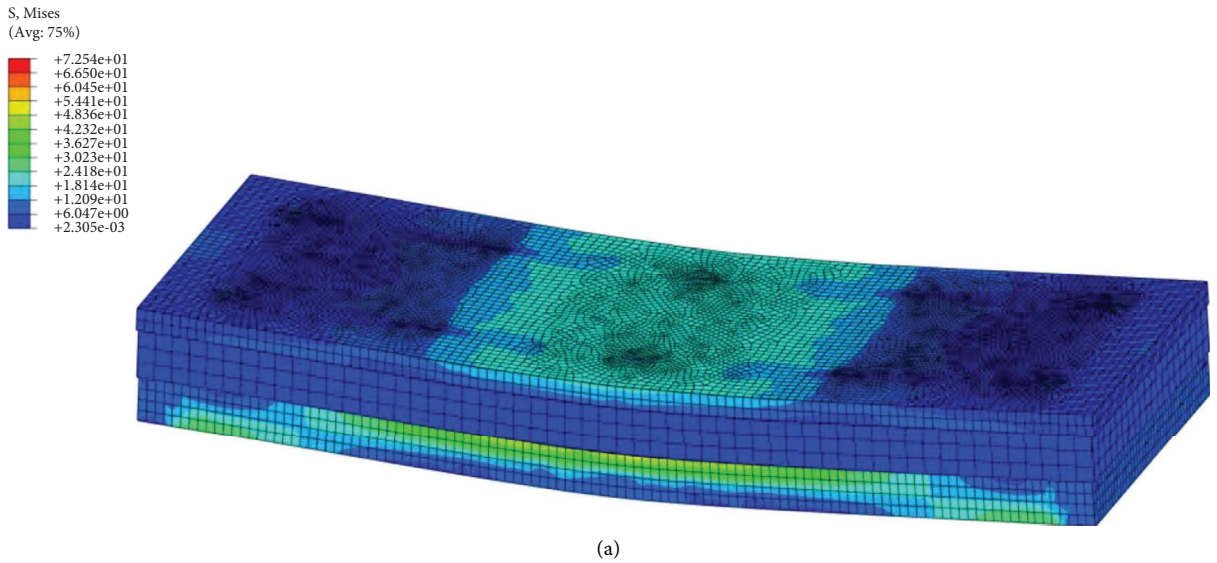

(a)

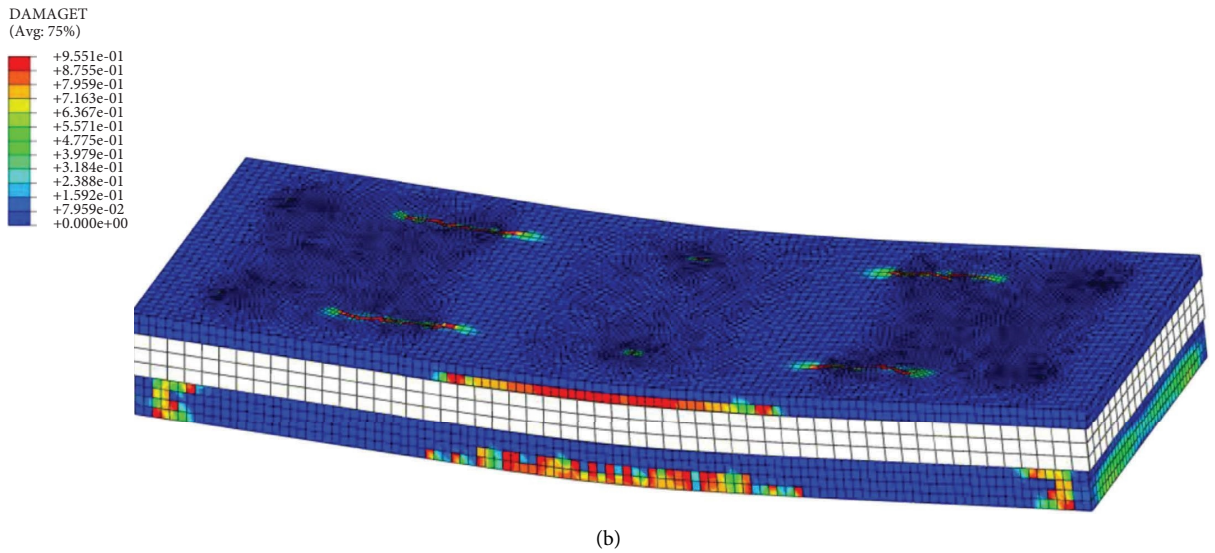

(b)

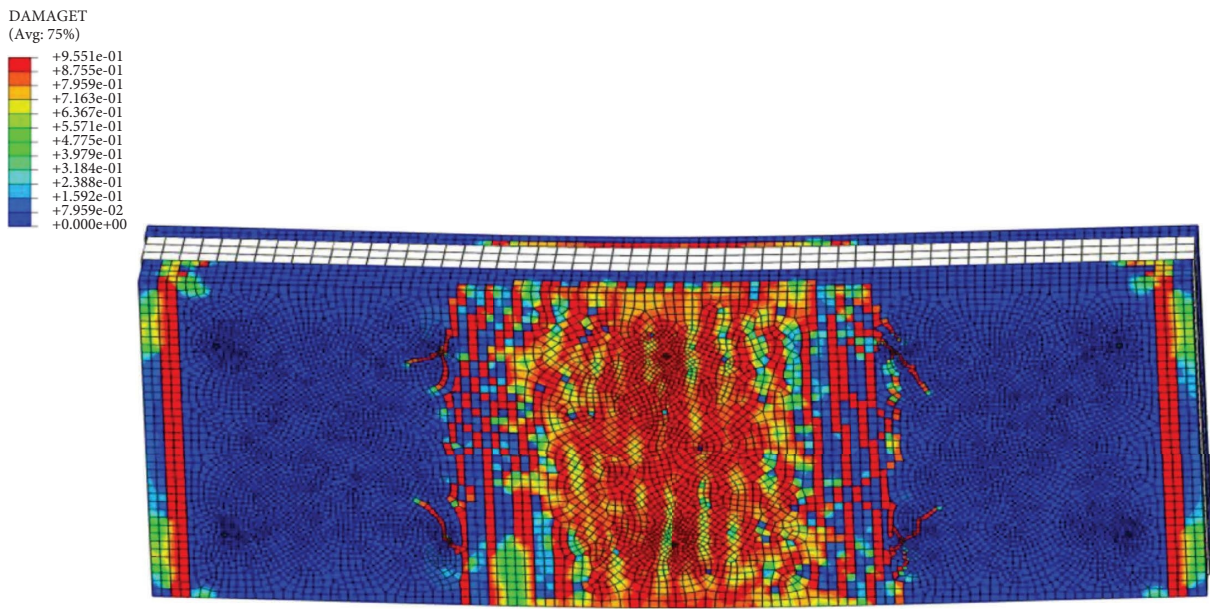

(c)

Figure 13: Continued.

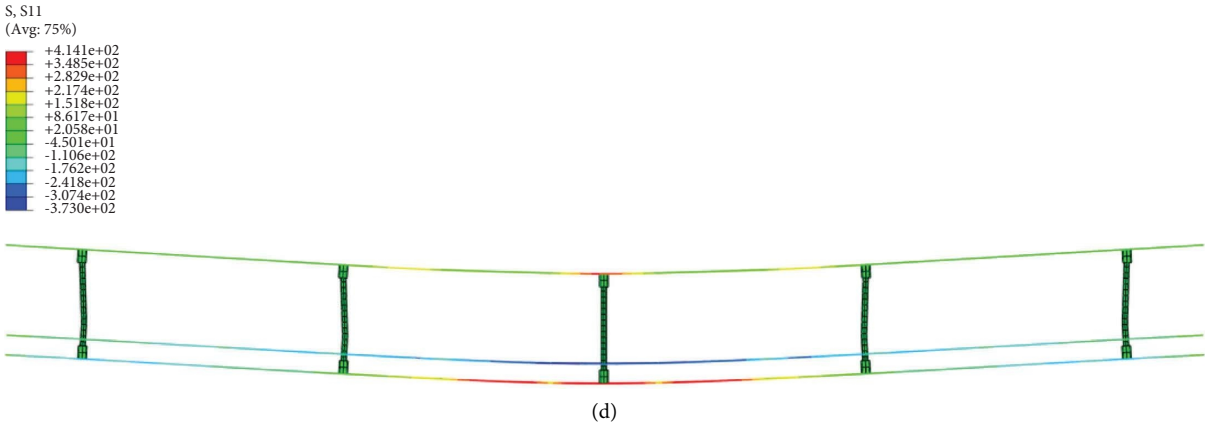

(d)

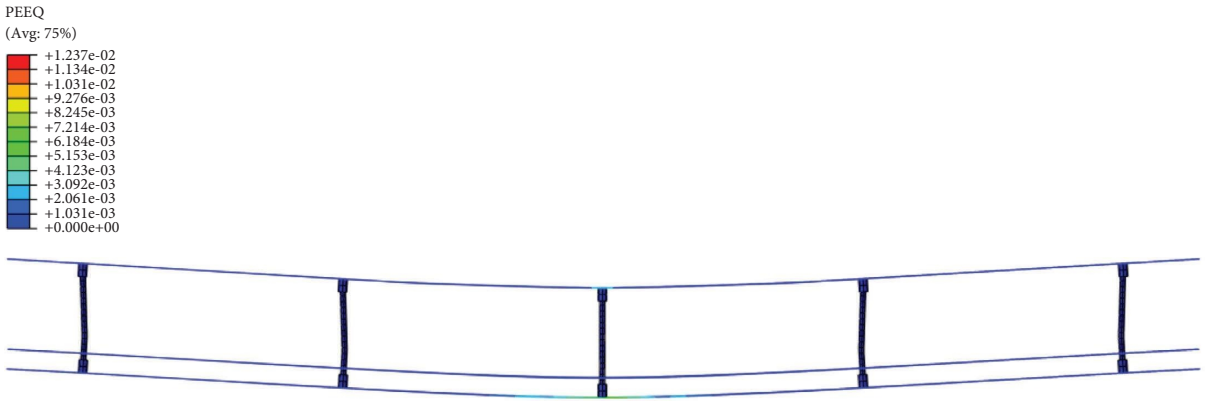

(e)

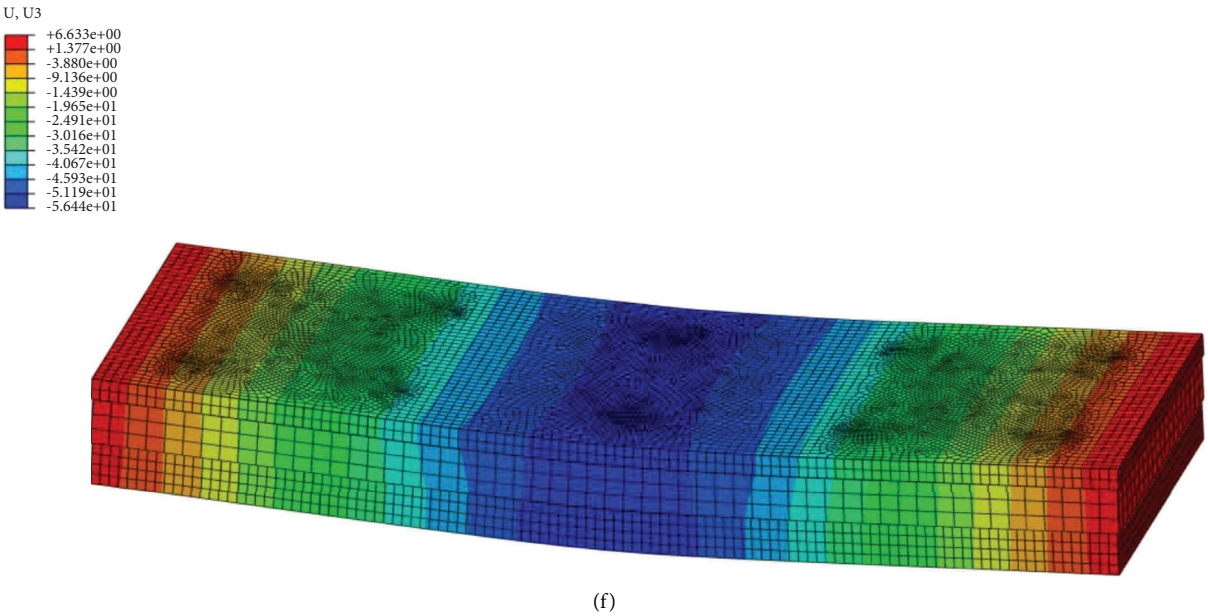

(f)

Figure 13: Simulated damage and contours of stress, strain, and displacement of G24A0.2-I at failure. (a) Stress contour of G24A0.2-I, (b) tension damage of G24A0.2-I, (c) tension damage on bottom wythe of G24A0.2-I, (d) stress contour of steel mesh of G24A0.2-I, (e) strain contour of steel mesh of G24A0.2-I, and (f) displacement contour of G24A0.2-I.

yielded in the midspan for both specimens of G24-I and G24A0.2-I. The FE model successfully captured the local buckling of the top wythe, tension damage on the bottom wythe, yield of longitudinal rebars in the bottom wythe, and deflection of test specimens.

The horizontal shear stress of the connectors of specimens G24-I and G24A0.2-I is shown in Figure 14. As mentioned in Reference [7], the shear strength was 20–25% of the tensile strength for GFRP bars, such that the shear strength of GFRP was taken as 95–119 MPa. The maximum horizontal shear stress in GFRP jackets of connectors was 72 and 88 Mpa for G24-I and G24A0.2-I, respectively, which were lower than the GFRP shear strength. Moreover, the shear strength of steel is ~50% of the tensile strength, such that the shear strength of the steel core was taken as 200 Mpa. The maximum horizontal shear stress in the steel core of connectors was 71 and 87 Mpa for G24-I and G24A0.2-I, respectively, which was lower than the shear strength of the steel core. These simulated results indicated that GFRP-steel hybrid shear connectors did not fail during the test.

A comparison between the experimental and numerical load-deflection curves for test specimens showed that the FE model offered a reasonable trend with the test data (Figure 15). That is to say that FE analyses were effective in capturing the shapes of the elastic and plastic phases of the measured load-deflection curves. The numerical ultimate loads were in good agreement with the test values (Table 7).

4.4. Influence of Arrangement of Shear Connectors. The verified FE model was used to analyze the influence of the arrangement of shear connectors on the flexural behavior of Sandwich panels. The spacing and number of shear connectors in Sandwich panel specimens were varied in the FE model, respectively (Figure 16). Three different spacings ($d = 550$, 600, and 650 mm) of connectors were tried in G24-I specimens. Also, four different numbers of shear connectors (=10, 12, 13, and 14) were used in these specimens, with the shear connectors arranged symmetrically. Specimens with different connector spacing had almost identical load-deflection curves (Figure 17(a)). The number of connectors had an insignificant influence on the stiffness of G24-I in the linear phase, while the ultimate loads of G24-I were enhanced up to 8% when the number of connectors increased from 10 (3.6/m^2) to 14 (5/m^2, Figure 17(b)).

5. Analytical Model of Sandwich Panel Deflection

In this section, the deflection of Sandwich panels with shear connectors under flexure was analysed based on the equilibrium equation of force, in which the effects of shear deflection, axial compression load, and slippage between the structural and facade wythes were considered.

This analysis was based on the following assumptions:

(1) The Sandwich panel section remains plane with respect to their neutral axes.

(2) Concrete in the tension region is ignored in the calculation of stiffness of cracked Sandwich panels.

(3) There is no relative slip between reinforcement and concrete in the compression region.

(4) The flexural resistance of the insulation foam core is ignored.

5.1. Stiffness of Sandwich Wall Panels. The effective moment of inertia of reinforced concrete wythes was calculated by transforming the wythe into a single type of material. Herein, the cross section of reinforced wythes was transformed into the concrete using a multiplier factor of moduli ratio of $\alpha_E = E_s/E_c$ (E_s and E_c are Young's moduli of steel and concrete, respectively).

For cracked Sandwich sections, the contribution of concrete in the tensile region is ignored. The depth of the neutral axis of cracked section y_{cr} was generated by summing the first moment of area about the neutral axis equal 0 (Figure 18).

With reference to Figure 18, there were two possible locations of the neutral axis to be considered:

Case 1. $a' < y_{cr} < h_{c1}$. The neutral axis lies inside the facade wythe. In this case, the following Equation can be applied:

$$\frac{by_{cr}^2}{2} + (\alpha_E - 1)A_s'(y_{cr} - a') = \frac{b(h_{c1} - y_{cr})^2}{2} + \alpha_E A_s (h_0 - y_{cr}), \tag{3}$$

where b is the width of the section, a' is the depth of the compressive reinforcement, h is the depth of the section, h_{c1} is the thickness of the facade wythe, h_0 is the effective depth of the section, and A_s and A_s' are the areas of steel reinforcements in tension and compression regions, respectively.

The cracking moment of inertia of the section I_{cr} can be obtained as follows:

$$I_{cr} = \frac{b}{3}\left[y_{cr}^3 + (h_{c1} - y_{cr})^3\right] + (\alpha_E - 1)A_s'(y_{cr} - a')^2 + \alpha_E A_s (h_0 - y_{cr})^2. \tag{4}$$

Case 2. $H_{c1} \le y_{cr} \le h_{c1} + h_e$. The neutral axis is located within the core. In this case, flexural stress in the core is ignored and the depth of the neutral axis of the cracked section y_{cr} is given by

$$bh_{c1}\left(y_{cr} - \frac{h_{c1}}{2}\right) + (\alpha_E - 1)A_s'(y_{cr} - a') = \alpha_E A_s (h_0 - y_{cr}). \tag{5}$$

The cracking moment of inertia of the section I_{cr} is thus given by

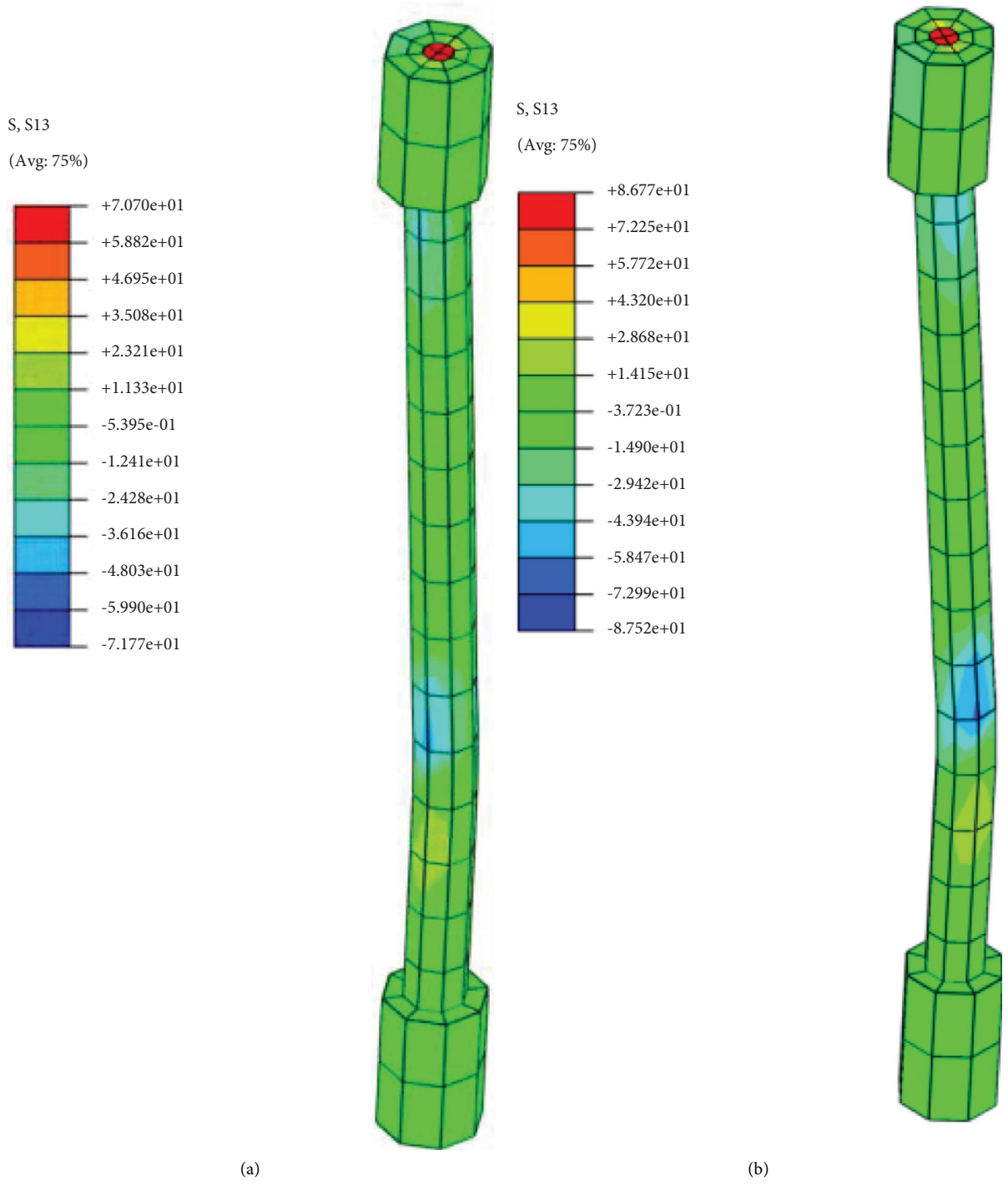

Figure 14: Simulated horizontal shear stress of connectors. (a) G24-I and (b) G24A0.2-I.

$$I_{cr} = \frac{bh_{c1}^3}{12} + bh_{c1}\left(y_{cr} - \frac{h_{c1}}{2}\right)^2 + (\alpha_E - 1)A_s'(y_{cr} - a')^2 + \alpha_E A_s(h_0 - y_{cr})^2. \quad (6)$$

The effective shear modulus for the Sandwich section, G_0, which includes the contribution of the wythes, can be defined based on the compliances of the constituent layers, as follows [39]:

$$\frac{h}{G_0} = \frac{h_{c1} + h_{c2}}{G_c} + \frac{h_f}{G_f}, \quad (7)$$

where, G_c and G_f are the shear moduli of the concrete and foam core, respectively, and h_{c2} and h_f are the

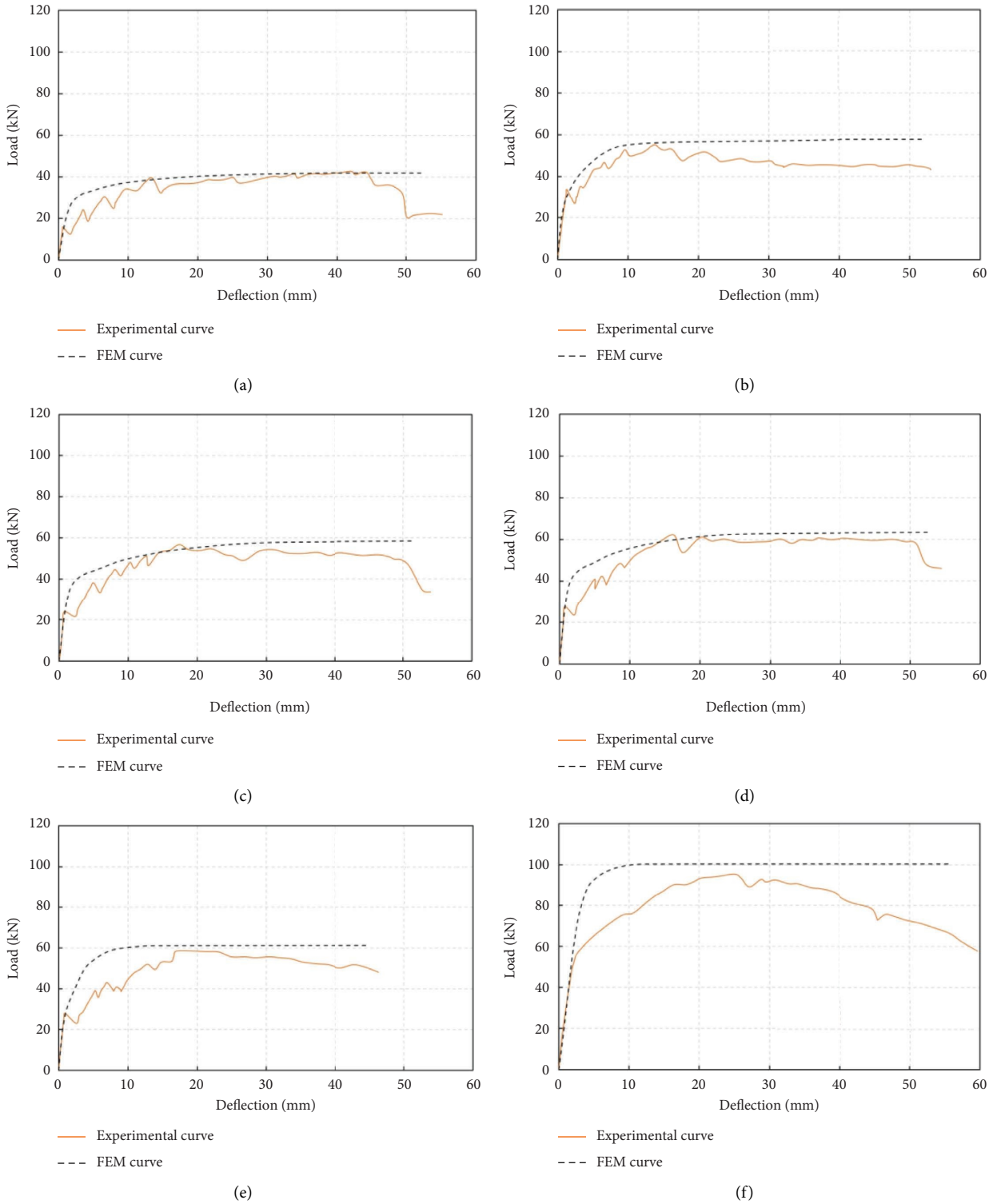

Figure 15: Continued.

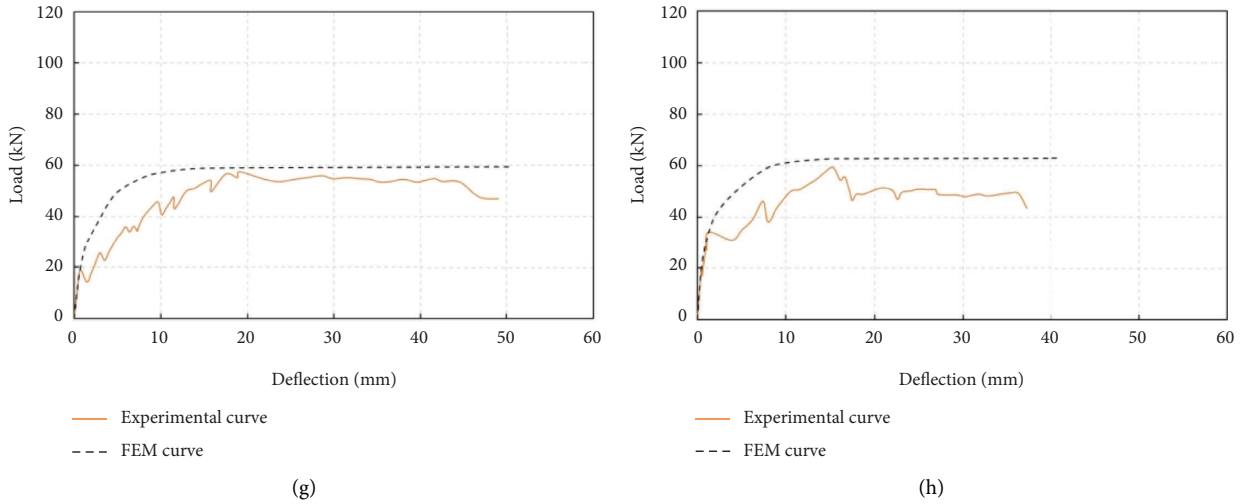

Figure 15: Comparison of numerical and experimental load-deflection curves. (a) G24-I, (b) G24-II, (c) G24S10-I, (d) G24S20-I, (e) G34-I, (f) G24A0.2-I, (g) G26-I, and (h) G26-II.

Table 7: Comparison of the ultimate load between numerical and experimental results.

Specimen	Tested ultimate load P_1 (kN)	Numerical ultimate load P_2 (kN)	$\delta = (P_2 - P_1/P_1) \times 100\%$
G24-I	39.44	41.97	6.4
G24-II	55.41	57.91	4.5
G24S10-I	56.66	58.46	3.2
G24S20-I	62.19	63.43	2.0
G24A0.2-I	95.25	100.4	5.4
G34-I	58.59	61.23	4.5
G26-I	57.45	59.50	3.6
G26-II	59.31	62.87	6.0

thicknesses of the structural wythe and the foam core, respectively.

5.2. Equilibrium Equation of Sandwich Wall Panels under Flexure. Due to the slippage between the structural and facade wythes, the sections of the structural and facade wythes are not in the same plane, so there is a neutral axis in either section of the structural and facade wythes. The distribution of strain and forces of the Sandwich panels are shown in Figure 19.

The flexural of the section will induce a resultant compressive force $C(x)$ in the concrete which acts through the centroid of the effective area of concrete in compression and a resultant tensile force $T(x)$ in the reinforcing steel is expressed as follows:

$$C(x) = y'' E_c A_1 d_1. \tag{8}$$

and

$$T(x) = y'' E_s A_s d_2, \tag{9}$$

where, A_1 is the area of the facade wythe, and d_1 and d_2 are the distances between the centroid of the facade and structural wythes to their neutral axes, respectively.

For equilibrium, the applied moment $M(x)$ is balanced by the moment of resistance of the section and resultant force $C(x)$ balanced by $T(x)$, such that

$$C(x) = T(x), \tag{10}$$

$$M(x) = y'' E_c I_1 + C(x)d. \tag{11}$$

and

$$d = d_0 + d_1 + d_2, \tag{12}$$

where, I_1 is the moment of inertia of the facade wythe, d is the distance between the centroids of the facade and structural wythes, and d_0 is the distance between neutral axes of the facade and structural wythes.

Due to the slippage between the facade and structural wythes, slip strain can be expressed as follows (Figure 19):

$$\varepsilon_e = \frac{ds}{dx}, \tag{13}$$

where, s is the relative slip of the facade and structural wythes.

The relationship between the slip strain and curvature is as follows:

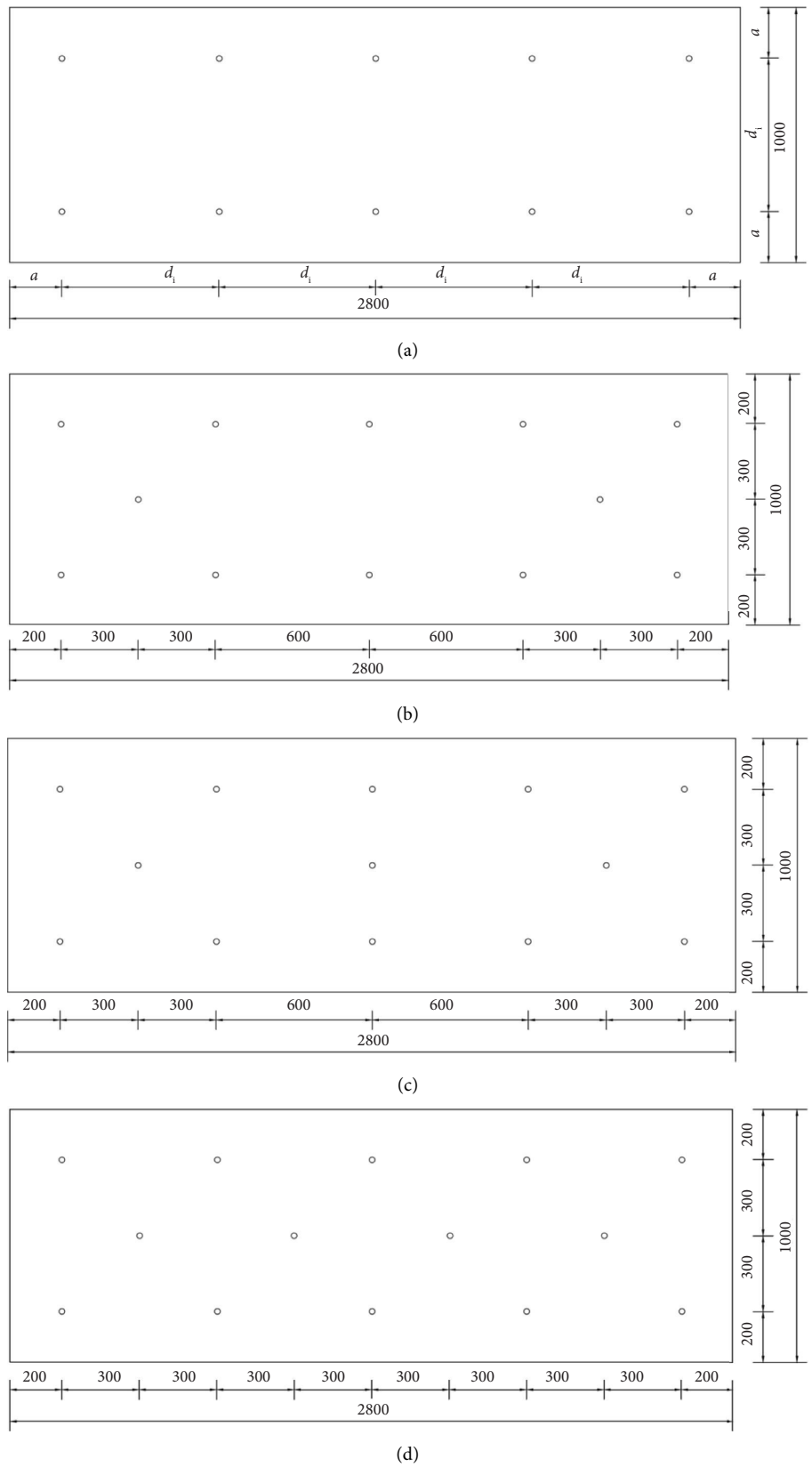

Figure 16: The arrangement of shear connectors tried in the FE model for specimen G24-I (units: mm). (a) The distance between shear connectors, (b) arrangement of 12 shear connectors, (c) arrangement of 13 shear connectors, and (d) arrangement of 14 shear connectors.

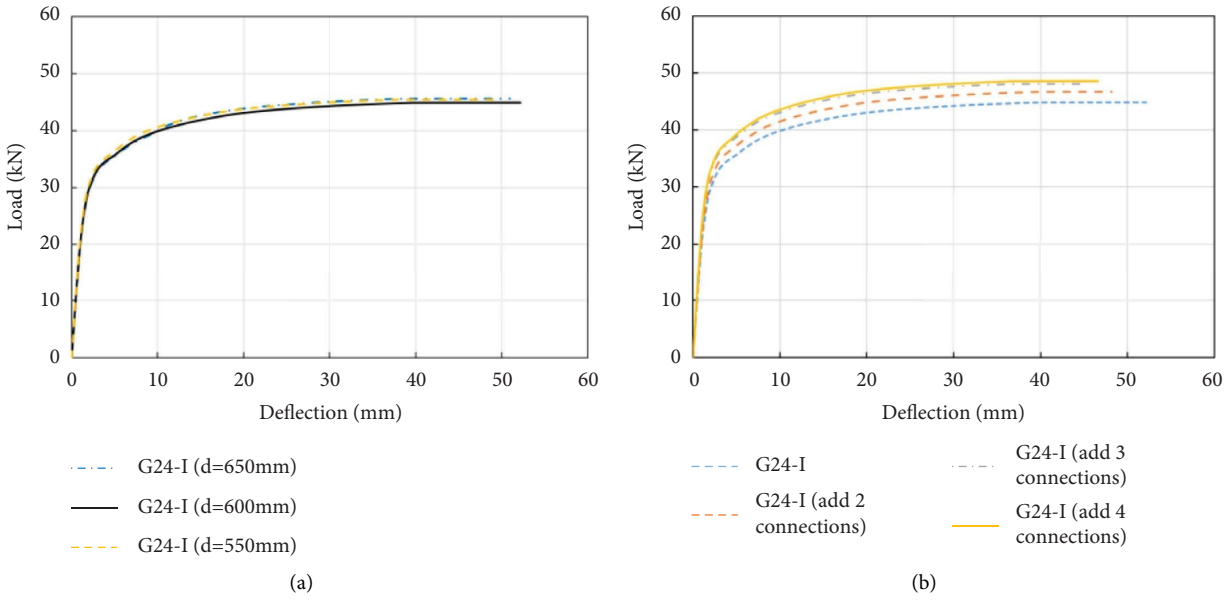

Figure 17: Simulated load-deflection curves of G24-I (a) with different distances between the shear connectors and (b) with the different number of shear connectors. (a) Influence of the distance between the connectors and (b) influence of the number of shear connectors.

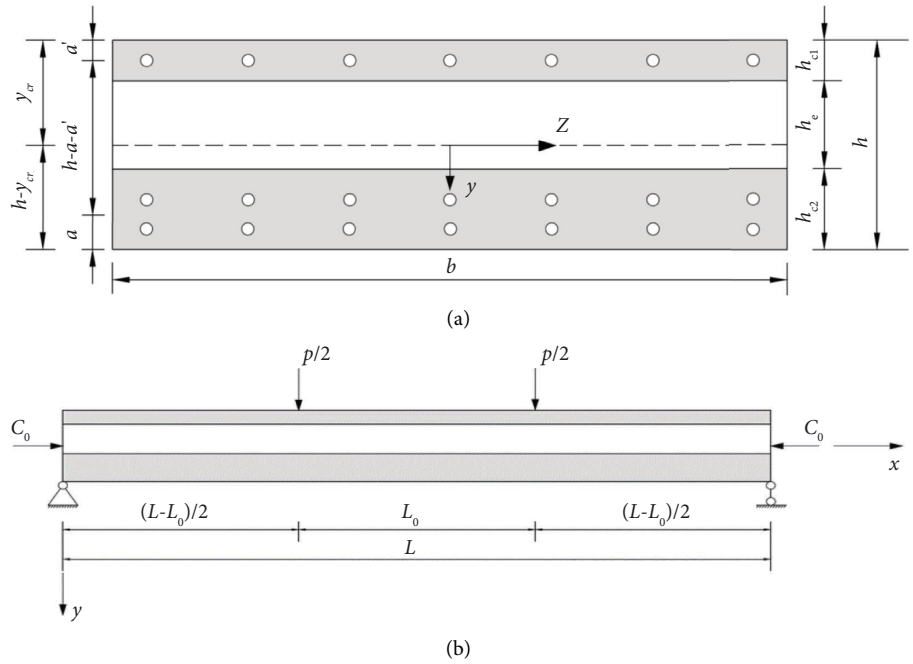

Figure 18: Coordinate system. (a) Cross section of sandwich panel and (b) side view of sandwich panel.

$$\varepsilon_e = y'' \cdot d_0. \tag{14}$$

Substituting (12) into (11) yielded

$$M(x) = \frac{I_1}{d}\left(y'' E_c d_1 + y'' E_c d_2\right) + \frac{E_c I_1}{d} y'' d_0 + C(x)d, \tag{15}$$

where, $C(x)$ is the axial force on the cross-section.

Then, substituting (8)–(10), (14) into (15) yielded,

$$M(x) = \frac{1+\alpha}{\alpha} C(x)d + \frac{E_c I_1}{d}\varepsilon_e, \tag{16}$$

where $\alpha = (\alpha_E A_s A_1 d^2/(A_1 + \alpha_E A_s) I_1)$.

The interface shear is proportional to the slip in the longitudinal direction, as given by

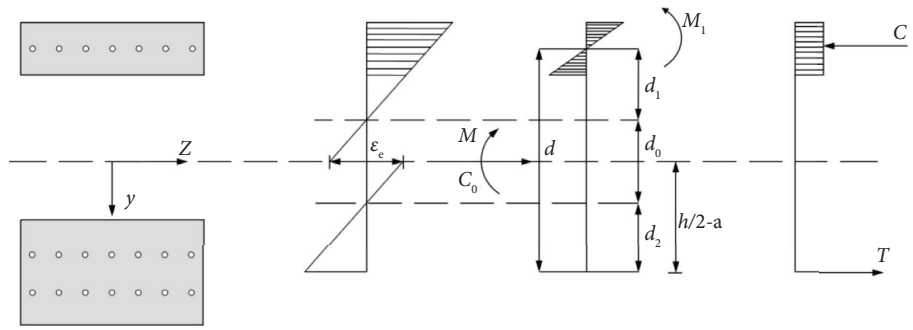

Figure 19: Distribution of strain and forces of sandwich panels.

$$q = Ks, \tag{17}$$

where, q is the interface shear per unit length in the longitudinal direction and K the shear stiffness of the connectors, as given by [40].

$$K = \frac{0.66 n_s N_u}{p}, \tag{18}$$

where, n_s is the number of connectors in the section, N_u is the shear capacity of the connector, and p is the distance of the connectors in the longitudinal direction of the panel.

Considering the element of facade wythe in Figure 20, the interface shear was equilibrated by the axial force, expressed as follows:

$$q = -\frac{\mathrm{d}C}{\mathrm{d}x}. \tag{19}$$

The substitution of (17) and (19) into (13) yielded

$$\varepsilon_e = \frac{1}{K} \cdot \left(-\frac{\mathrm{d}^2 C}{\mathrm{d}x^2} \right). \tag{20}$$

Then, substituting (20) into (16) yielded

$$C''(x) = \frac{(1+\alpha) d^2 K}{\alpha E_c I_1} C(x) - \frac{K d}{E_c I_1} M(x). \tag{21}$$

For specimens under four-point flexure, the applied moment of the section is as follows:

$$M(x) = \frac{Px}{2}, \quad \left(0 \le x \le \frac{L - L_0}{2} \right). \tag{22}$$

and

$$M(x) = \frac{P(L - L_0)}{4}, \quad \left(\frac{L - L_0}{2} < x \le \frac{L}{2} \right), \tag{23}$$

where L is the clear span of the panel and L_0 is the distance between two vertical loads.

There was no relative slip between the facade and structural wythes in the midspan section because the specimen was symmetric with respect to the midspan section, such that $s(L/2) = q(L/2) = 0$.

Substituting (22) and (23) into (21) and considering the fact that $C(0) = 0$ and $C'(L/2) = 0$, axial force in the facade wythe was obtained as follows:

$$C(x) = \frac{\left(e^{\omega L_1} + e^{\omega L - \omega L_1} \right) \alpha P}{4(1+\alpha)\left(1 + e^{\omega L}\right) \omega d} \left(e^{-\omega x} - e^{\omega x} \right) + \frac{\alpha P}{2(1+\alpha) d} x, \quad (0 \le x \le L1). \tag{24}$$

and

$$C(x) = \frac{\left(e^{-\omega L_1} - e^{\omega L_1} \right) \alpha P}{4(1+\alpha)\left(1 + e^{\omega L}\right) \omega d} \left(e^{\omega L - \omega x} + e^{\omega x} \right) + \frac{\alpha P L_1}{2(1+\alpha) d}, \quad \left(L1 \le x \le \frac{L}{2} \right), \tag{25}$$

where $\omega^2 = ((1+\alpha) d^2 K / \alpha E_c I_1)$.

5.3. Deflection of Sandwich Panels under Flexure. If the edge is simply supported, the deflections $y(0)$ and $y(L)$ were zero. Substituting (24) and (25) into (11) and considering the boundary conditions, the deflection of the midspan section $y_0(L/2)$ was thus obtained as follows:

$$y_0\left(\frac{L}{2}\right) = \frac{P L_1 \left(3L^2 - 4L_1^2 \right)}{48 E_c I} + \frac{2\beta L_1}{\omega^2 E_c I_1} + \frac{2\beta}{\omega^3 E_c I_1} \cdot \frac{e^{(\omega L/2) - \omega L_1} - e^{(\omega L/2) + \omega L_1}}{1 + e^{\omega L}}, \tag{26}$$

where $\beta = (\alpha P / 4(1+\alpha))$ and $I = \kappa_2 I_1 (1+\alpha)$.

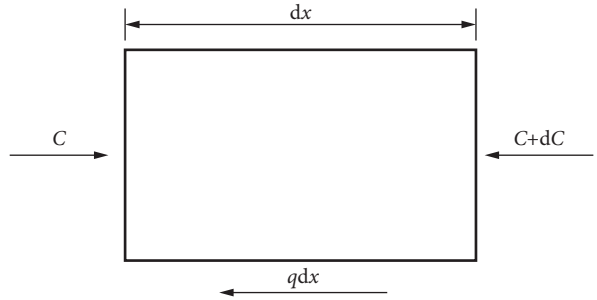

Figure 20: The element diagram of the façade wythe.

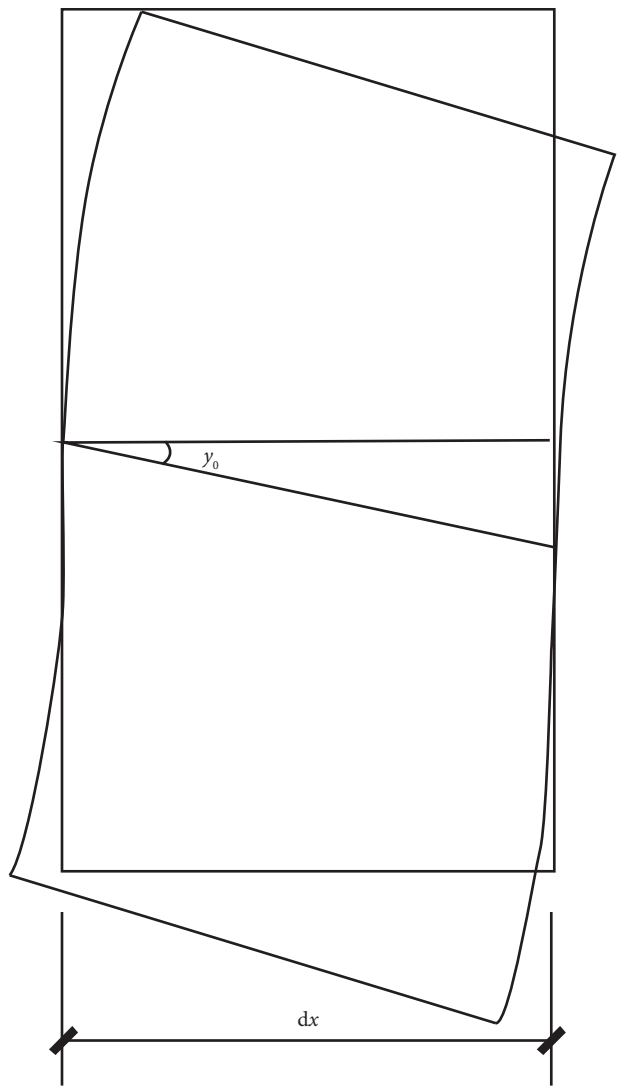

Figure 21: Shear deformation of the element of sandwich panels.

Table 8: Comparison of the maximum deflection between analytical and experimental results.

Specimen	Tested deflection y_1 (mm)	Analytical deflection y_2 (mm)	δ (%)
G24-I	13.47	14.19	5.31
G24-II	13.88	15.78	13.68
G24S10-I	17.41	16.35	−6.06
G24S20-I	16.22	16.97	4.61
G24A0.2-I	25	25.00	0.01
G34-I	16.98	15.30	−9.89
G26-I	19.05	16.47	−13.54
G26-II	15.33	16.13	5.23

Considering an element of the panel cut out by two adjacent cross-sections with a distance dx apart (Figure 21), the relationship between the shear deflection and shear force was given by [41]

$$\begin{aligned}\frac{dy_s}{dx} &= \gamma_0 \\ &= \frac{\alpha_s V}{G_0 A},\end{aligned} \tag{27}$$

where, y_s is the shear deflection, γ_0 is the shear strain at the centroid of cross-sections, α_s is a numerical factor with which the average shearing stress must be multiplied in order to obtain the shearing stress at the centroid of cross-sections ($\alpha_s = (3/2)$ for a rectangular cross-section and $\alpha_s = (4/3)$ for a circular cross-section), V is the section shear force, and A is the section area.

The shear deflection of the Sandwich panel was obtained by integrating (27) over half of the panel span and the shear deflection of the midspan section thus given by

$$\begin{aligned}y_s\left(\frac{L}{2}\right) &= \frac{2\alpha_s}{G_0 A}\int_0^{\frac{L}{2}} V\,dx \\ &= \frac{2\alpha_s}{G_0 A}\cdot\frac{PL_1}{2L}\cdot\frac{L}{2} \\ &= \frac{\alpha_s PL_1}{2G_0 A}.\end{aligned} \tag{28}$$

Adding Eq. (28) to (26), the deflection at the midspan of the Sandwich panels under flexure was expressed as follows:

$$\begin{aligned}y_0'\left(\frac{L}{2}\right) &= \frac{PL_1\left(3L^2-4L_1^2\right)}{48E_c I} + \frac{2\beta L_1}{\omega^2 E_c I_1} \\ &\quad + \frac{2\beta}{\omega^3 E_c I_1}\cdot\frac{e^{(\omega L/2)-\omega L_1} - e^{(\omega L/2)+\omega L_1}}{1+e^{\omega L}} + \frac{\alpha_s PL_1}{2G_0 A},\end{aligned} \tag{29}$$

in which the effects of slipping and shear deflection were included.

5.4. Deflection of Sandwich Panels Under Combined Axial-Flexural Loading. For specimens under the combined effects of flexure and compression, no slipping occurred between the facade and structural wythes. Hence, the deflection of the mid-span section was given by [42]

$$y\left(\frac{L}{2}\right) = \frac{PL_1\left(3L^2-4L_1^2\right)}{48E_c I}\chi(u), \tag{30}$$

where $u = (L/2)\sqrt{(C_0/E_c I)}$, $\chi(u) = (3(\tan u - u)/u^3)$, and C_0 are the applied axial compressive load.

Considering the effect of shear deflection, the deflection at the midspan of Sandwich panels subjected to combined axial-flexural loads was obtained by adding Equation (28) to (30), yielding

$$y'\left(\frac{L}{2}\right) = \frac{PL_1\left(3L^2-4L_1^2\right)}{48E_c I}\chi(u) + \frac{\alpha_s PL_1}{2G_0 A}. \tag{31}$$

5.5. Comparison of Analytical and Experimental Results. Equation (29) was used to calculate the deflection at the ultimate load for the insulated concrete Sandwich panels under flexure. Equation (31) was used to calculate the deflection at the ultimate load for the insulated concrete Sandwich panels under the combined effects of flexure and compression. Comparisons of the analytical and measured deflections at the ultimate load at midspan of test specimens showed good agreement (Table 8).

6. Conclusions

The structural responses of insulated concrete sandwiches with innovative dumbbell-shaped SFCB connectors under flexural load were investigated. The results obtained from this study were summarized as follows:

(1) The failure modes of Sandwich panel specimens under positive flexure were governed by the yielding of the tension rebars and penetrating of the bottom wythe in the midspan. The thickness of GFRP on the hybrid bars, raised thickness of the dumbbells, and the content of vitrified microspheres have insignificant influences on the failure modes of Sandwich panel specimens. These specimens, under combined axial-flexural loads, exhibited different failure modes from specimens without axial loads, in which the axial compressive load delayed crack onset in the bottom concrete wythe and prevented slipping between the facade and structural wythes. The failure modes of specimens under negative flexure were similar to those of specimens with an axial compression ratio of 0.2/1.

(2) The increase in thickness of the GFRP jacket on the hybrid bar from 2 to 3 mm led to increased initial cracking load, ultimate load, and flexural stiffness of specimens by 75, 49, and 16%, respectively. The increase in raised thickness of dumbbell ends from 4 to 6 mm led to increased initial cracking load, ultimate load, and flexural stiffness of specimens of 18,

46, and 9%, respectively. Both the increased thickness of the GFRP jacket and raised thickness of dumbbell ends contributed to decreased slip between the two wythes but had insignificant influence on ductility. The incorporation of vitrified microspheres in concrete wythes resulted in a remarkable increase in the load-carrying capacity of the Sandwich panels but decreased ductility. Increased axial compression ratio from 0/1 to 0.2/1 contributed in improving crack resistance and ultimate loads of these panels. No slip occurred in specimens under combined axial-flexural loading. Specimens under negative flexure had higher ultimate load and lower ductility than their counterpart under positive flexure.

(3) The FE model provided a reasonable simulation of the experimental results. Moreover, the verified FE model was used to analyze the influence of the arrangement of shear connectors. It is found that increasing the spacing of the connectors from 550 to 650 mm had an insignificant influence on the load-deflection responses and increasing the number of shear connectors per square meter from 3.6 to 5 led to a slight increase (~8%) in the ultimate load.

(4) Based on the relationship between slip strain and curvature and considering the relationship between interface shear and slip, the equilibrium equation of the composite section under flexure was solved to obtain the deflection of sandwich panel specimens, in which the effect of shear deflection and slipping between the two wythes were included. For specimens under the combined axial-flexural loads, no slipping effect was included in the analytical solution. A comparison of analytical and test results showed that deflection at the ultimate load was accurately predicted by the proposed theoretical model.

(5) To promote the application of the sandwich wall panels with these innovative dumbbell-shaped SFCB connectors in building engineering, further research will be needed to optimize the configuration sandwich wall panels and investigate the thermal and seismic performances of the sandwich wall panel.

Data Availability

Data will be made available on request.

Conflicts of Interest

The authors declare that they have no conflicts of interest regarding the publication of this article.

Authors' Contributions

Yi Wang performed numerical analysis, validation, experimental study, and wrote the original draft. Jun Wang carried out conceptualization, formal analysis, resources, and project administration. Donghui Zhao performed data curation andinvestigation. Hota Gangarao carried out methodology and reviewed and edited the study. Ruifeng Liang performed the analysis of failure mode. David Hui visualized the study.

Acknowledgments

The financial support was received from the https://doi.org/10.13039/501100001809 National Natural Science Foundation of China (Grant 52278261) and the Science and Technology Project of Jiangsu Construction System, China (Grant 2021ZD05).

References

[1] P. Syndergaard, R. Tawadrous, S. Al-Rubaye, and M. Maguire, "Comparing testing methods of partially composite sandwich wall panel glass fiber-reinforced polymer connectors," *Journal of Composites for Construction*, vol. 26, no. 1, Article ID 04021070, 2022.

[2] J. Xie, F. Chen, J. Zhao, P. Lu, F. Liu, and L. Li, "Flexural behaviour of full-scale precast recycled concrete sandwich panels with BFRP connectors," *Journal of Building Engineering*, vol. 56, Article ID 104816, 2022.

[3] B. Egbon and D. Tomlinson, "Experimental investigation of longitudinal shear transfer in insulated concrete wall panels with notched insulation," *Journal of Building Engineering*, vol. 43, Article ID 103173, 2021.

[4] H. L. Xie, H. Fang, W. Cai, L. Wan, R. L. Huo, and D. Hui, "Development of an innovative composite sandwich matting with GFRP facesheets and wood core," *Reviews on Advanced Materials Science*, vol. 60, no. 1, pp. 80–91, 2021.

[5] K. Huang, J. Xie, R. Wang, Y. Feng, and R. Rao, "Effects of the combined usage of nanomaterials and steel fibres on the workability, compressive strength, and microstructure of ultra-high performance concrete," *Nanotechnology Reviews*, vol. 10, no. 1, pp. 304–317, 2021.

[6] S. Yu, Y. Liu, D. Wang, C. Ma, and J. Liu, "Theoretical, experimental and numerical study on the influence of connectors on the thermal performance of precast concrete sandwich walls," *Journal of Building Engineering*, vol. 57, Article ID 104886, 2022.

[7] G. Woltman, D. Tomlinson, and A. Fam, "Investigation of various GFRP shear connectors for insulated precast concrete sandwich wall panels," *Journal of Composites for Construction*, vol. 17, no. 5, pp. 711–721, 2013.

[8] A. Chen, T. G. Norris, P. M. Hopkins, and M. Yossef, "Experimental investigation and finite element analysis of flexural behavior of insulated concrete sandwich panels with FRP plate shear connectors," *Engineering Structures*, vol. 98, pp. 95–108, 2015.

[9] D. G. Tomlinson, N. Teixeira, and A. Fam, "New shear connector design for insulated concrete sandwich panels using basalt fiber-reinforced polymer bars," *Journal of Composites for Construction*, vol. 20, no. 4, Article ID 04016003, 2016.

[10] R. Lameiras, I. B. Valente, J. A. O. Barros, M. Azenha, and C. Gonçalves, "Pull-out behaviour of Glass-Fibre Reinforced Polymer perforated plate connectors embedded in concrete. Part I: experimental program," *Construction and Building Materials*, vol. 162, pp. 155–169, 2018.

[11] W. Choi, S. J. Jang, and H. D. Yun, "Design properties of insulated precast concrete sandwich panels with composite shear connectors," *Composites Part B: Engineering*, vol. 157, pp. 36–42, 2019.

[12] Z. Z. He, P. Pan, Y. M. Guo, Y. R. Cao, S. D. Shen, and B. B. Ye, "Pull-out and shear tests of long glass FRP connector for sandwich-insulation wall panels," *Journal of Composites for Construction*, vol. 25, no. 5, Article ID 04021047, 2021.

[13] D. Chen, K. K. Li, Z. Y. Yuan, B. Q. Cheng, and X. Kang, "Shear behavior of FRP connectors in precast sandwich insulation wall panels," *Buildings*, vol. 12, no. 8, p. 1095, 2022.

[14] Z. Z. He, P. Pan, G. Q. Xiao, S. D. Shen, and J. Y. Ren, "Test and analysis on axial performances of GFRP restraint connectors for sandwich insulation wall panels," *Journal of Building Engineering*, vol. 45, Article ID 103457, 2022.

[15] J. Q. Huang, Y. Y. Xu, H. Huang, and J. G. Dai, "Structural behavior of FRP connector enabled precast geopolymer concrete sandwich panels subjected to one-side fire exposure," *Fire Safety Journal*, vol. 128, Article ID 103524, 2022.

[16] G. Wu, Z. S. Wu, Y. B. Luo, Z. Y. Sun, and X. Q. Hu, "Mechanical properties of steel-FRP composite bar under uniaxial and cyclic tensile loads," *Journal of Materials in Civil Engineering*, vol. 22, no. 10, pp. 1056–1066, 2010.

[17] D. B. Cleary, W. T. Riddell, N. Camishion et al., "Steel connections with fiber-reinforced resin thermal barrier filler plates under service loading," *Journal of Structural Engineering*, vol. 142, no. 11, Article ID 04016095, 2016.

[18] Z. Dong, G. Wu, and Y. Xu, "Experimental study on the bond durability between steel-FRP composite bars (SFCBs) and sea sand concrete in ocean environment," *Construction and Building Materials*, vol. 115, pp. 277–284, 2016.

[19] D. W. Seo, K. T. Park, Y. J. You, and S. Y. Lee, "Experimental investigation for tensile performance of GFRP-steel hybridized rebar," *Advances in Materials Science and Engineering*, vol. 2016, Article ID 9401427, 12 pages, 2016.

[20] Q. Zhi and Z. X. Guo, "Experimental evaluation of precast concrete sandwich wall panels with steel-glass fiber-reinforced polymer shear connectors," *Advances in Structural Engineering*, vol. 20, no. 10, pp. 1476–1492, 2017.

[21] Y. Zhou, Y. Zheng, J. Pan et al., "Experimental investigations on corrosion resistance of innovative steel-FRP composite bars using X-ray microcomputed tomography," *Composites Part B: Engineering*, vol. 161, pp. 272–284, 2019.

[22] Y. Yang, Z. Y. Sun, G. Wu, D. F. Cao, and D. Pan, "Experimental study of concrete beams reinforced with hybrid bars (SFCBs and BFRP bars)," *Materials and Structures*, vol. 53, no. 4, p. 77, 2020.

[23] W. J. Ge, Y. M. Wang, A. R. A. Ashour, W. G. Lu, and D. F. Cao, "Flexural performance of concrete beams reinforced with steel-FRP composite bars," *Archives of Civil and Mechanical Engineering*, vol. 20, no. 2, p. 56, 2020.

[24] W. Ge, K. Chen, Z. Guan, A. Ashour, W. Lu, and D. Cao, "Eccentric compression behaviour of concrete columns reinforced with steel-FRP composite bars," *Engineering Structures*, vol. 238, Article ID 112240, 2021.

[25] C. Su, X. Wang, L. Ding, Z. Chen, S. Liu, and Z. Wu, "Experimental study on the seismic behavior of seawater sea sand concrete beams reinforced with steel-FRP composite bars," *Engineering Structures*, vol. 248, Article ID 113269, 2021.

[26] P. Pan, Z. Z. He, H. S. Wang, and Y. J. Kang, "Experimental investigation of C-shaped glass-fiber-reinforced polymer connectors for sandwich insulation wall panels," *Engineering Structures*, vol. 250, Article ID 113462, 2022.

[27] GB/T 228.1-2010, *Metallic Materials - Tensile Testing - Part 1: Method of Test at Room Temperature*, Standards Press of China, Beijing, China, 2010.

[28] J. G./T 406-2013, *Glass Fibre Reinforced Plastics Rebar for Civil Engineering*, Standards Press of China, Beijing, China, 2013.

[29] Gb/T. 50081-2019, *Standard for Test Methods of concrete Physical and Mechanical Properties*, China Architecture & Building Press, Beijing, China, 2019.

[30] Y. Zhang, G. Ma, Z. F. Wang, Z. Niu, Y. Z. Liu, and Z. Li, "Shear behavior of reinforced glazed hollow bead insulation concrete beams," *Construction and Building Materials*, vol. 174, pp. 81–95, 2018.

[31] L. Zhao, W. Wang, Z. Li, and Y. F. Chen, "An experimental study to evaluate the effects of adding glazed hollow beads on the mechanical properties and thermal conductivity of concrete," *Materials Research Innovations*, vol. 19, no. 5, pp. S5-S929–S5-935, 2015.

[32] O. Gunes, D. Lau, C. Tuakta, and O. Büyüköztürk, "Ductility of FRP-concrete systems: investigations at different length scales," *Construction and Building Materials*, vol. 49, pp. 915–925, 2013.

[33] I. Choi, J. Kim, D. Kim, and J. Park, "Effects of grid-type shear connector arrangements used for insulated concrete sandwich wall panels with a low aspect ratio," *Journal of Building Engineering*, vol. 46, Article ID 103754, 2022.

[34] I. Choi, J. Kim, and H. R. Kim, "Composite behavior of insulated concrete sandwich wall panels subjected to wind pressure and suction," *Materials*, vol. 8, no. 3, pp. 1264–1282, 2015.

[35] GB 50010-2010, *Code for Design of concrete Structures*, China Architecture & Building Press, Beijing, China, 2015.

[36] L. Qingfu, G. Wei, and K. Yihang, "Parameter calculation and verification of concrete plastic damage model of ABAQUS," *IOP Conference Series: Materials Science and Engineering*, vol. 794, no. 1, Article ID 012036, 2020.

[37] L. Godrich, F. Wald, J. Kabelac, and M. Kurikova, "Design finite element model of a bolted T-stub connection component," *Journal of Constructional Steel Research*, vol. 157, pp. 198–206, 2019.

[38] H. Jiang and M. G. Chorzepa, "Evaluation of a new FRP fender system for bridge pier protection against vessel collision," *Journal of Bridge Engineering*, vol. 20, no. 2, Article ID 05014010, 2015.

[39] L. A. Carlsson and G. A. Kardomateas, *Structural and Failure Mechanics of Sandwich Composites*, Springer Netherlands, Dordrecht, Netherlands, 2011.

[40] H. Yuan, Y. Yang, H. Deng, Y. Weijian, and P. Bo, "Element-based stiffness reduction coefficient of steel–concrete composite beams with interface slip," *Materials and Structures*, vol. 49, no. 12, pp. 5021–5029, 2016.

[41] S. P. Timoshenko, *Strength of Materials. Part I: Elementary Theory and Problems*, D Van Nostrand Company Inc, New York, NY, USA, 1940.

[42] S. P. Timoshenko and J. M. Gere, *Theory of Elastic Stability*, Mcgraw-Hill International Book Company Inc, New York, NY, USA, 1961.